Airborne investigation of black carbon interaction with low-level, persistent, mixed-phase clouds in the Arctic summer

Marco Zanatta[1,2], Stephan Mertes[3], Olivier Jourdan[4], Regis Dupuy[4], Emma Järvinen[2], Martin Schnaiter[2], Oliver Eppers[5,6], Johannes Schneider[5], Zsófia Jurányi[1], Andreas Herber[1]

[1]Alfred-Wegener-Institut, Helmholtz-Zentrum für Polar- und Meeresforschung (AWI), Bremerhaven, Germany

[2]Institute of Meteorology and Climate Research, Karlsruhe Institute of Technology, Karlsruhe, Germany

[3]Leibniz-Institut für Troposphärenforschung, Leipzig, Germany

[4]Laboratoire de Météorologie Physique, Université Clermont Auvergne/OPGC/CNRS, UMR 6016, Clermont-Ferrand, France

[5]Particle Chemistry Department, Max Planck Institute for Chemistry, Mainz, Germany

[6]Institute for Atmospheric Physics, University of Mainz, Mainz, Germany

Correspondence to: Marco Zanatta (marco.zanatta@kit.edu)

Changes

Reviewer1   Reviewer2   General

Abstract. Aerosol-cloud interaction is considered one of the largest sources of uncertainties in radiative forcing estimations. To better understand the role of black carbon aerosol as cloud nucleus and the impact of clouds on its vertical distribution in the Arctic, we report airborne in-situ measurements of refractory black carbon aerosol particles (rBC) in the European Arctic near Svalbard during the ACLOUD campaign held in summer 2017. rBC was measured with a single particle soot photometer on board of the research aircraft "Polar 6" from the lowest atmospheric layer up to approximately 3500 m asl. During in-cloud flight transects, rBC particles contained in liquid droplets (rBC-residuals) were sampled through a counterflow virtual impactor (CVI). Four flights conducted in the presence of inside-inversion, surface-coupled, mixed-phase clouds over sea ice, were selected to address the variability of rBC particles sampled above, below and within the cloud layer. First, the increase of size and coating thickness of rBC particles from the free troposphere to the cloud-dominated boundary layer confirmed that ground observations are not representative of upper atmospheric layers. Second, although only 1% of liquid droplets contained an rBC particle, the higher number concentration of rBC-residuals than rBC particles sampled below-cloud indicated that the totality of below-cloud rBC was activated by nucleation scavenging, but also that alternative scavenging processes such as activation of free-tropospheric rBC at the cloud-top might occur. Third, the efficient exchange of aerosol at cloud-bottom was confirmed by the similarity of rBC-residuals size distribution to below-cloud conditions. Last, the increase of rBC-residuals number

concentration (+31%) and geometric mean diameter (+38%) from cloud-top to cloud-bottom and the absolute enrichment of larger rBC-residuals compared to outside-cloud, supported the hypothesis of concomitant scavenging mechanisms but also suggested the formation of rBC agglomerates caused by cloud-processing. The vertical evolution of rBC properties from inside-cloud and below-cloud indicated an efficient aerosol exchange at cloud-bottom, which might include activation, cloud processing, and sub-cloud release of processed rBC agglomerates. In the case of persistent low-level Arctic clouds, this cycle may reiterate multiple times, adding one additional degree of complexity to the understanding of cloud processing of black carbon particles in the Arctic.

1   Introduction

It is well known that clouds strongly impact the surface energy budget in the Arctic (Shupe and Intrieri, 2004; Lubin and Vogelmann, 2006). However, the interaction between aerosol particles and clouds remains one of the major sources of uncertainty in radiative forcing estimations, not only in the Arctic but on a global scale as well (Bellouin et al., 2020; IPCC et al., 2021).

Black carbon (BC) particles are carbonaceous aerosol particles emitted by incomplete combustion of fossil fuels and biomasses (Bond et al., 2004) and, due to their unique absorption of solar radiation in the visible spectrum, they play an important role in the Arctic radiative balance. First, BC particles directly interact with the solar radiation causing a net warming of its atmospheric layer (Flanner, 2013). Second, the change in local temperature might influence cloud's vertical distribution via semi-direct effects (Sand et al., 2013). Third, via aerosol-cloud interaction, also known as the first indirect effect, black carbon activation might lead to a change in the microphysical properties of clouds with consequences on cloud radiative properties (Sand et al., 2013). Lastly, after deposition, BC can decrease the snow albedo promoting melting via the snow darkening effect (Flanner et al., 2009). All these processes are strongly interconnected (Quinn et al., 2015), making BC the third atmospheric Arctic warmer only after the trace gases carbon dioxide and methane (Oshima et al., 2020).

The seasonality of BC concentration at the Arctic surface is characterized by a maximum in the early spring and a minimum in summer (Quinn et al., 2015). A similar seasonality was also recently reported on the vertical scale (Jurányi et al., 2023). Due to the scarcity of BC sources within the Arctic, most of BC mass reaches the Arctic via long range transport (Xu et al., 2017). Hence, the seasonal cycle is mostly controlled by the circulation of air masses between the Arctic and southern latitudes (Bozem et al., 2019), and by precipitation during long-range transport (Croft et al., 2016). Hence, the ability of BC to interact with clouds (cloud scavenging) is particularly relevant to asses BC burden and radiative forcing in the Arctic region. Overall, cloud scavenging is responsible of 90% of BC mass deposition in the Arctic (Dou and Xiao, 2016), with the highest precipitation rate in summer contributing to a decline of BC burden from late spring to autumn (Garrett et al., 2011; Mori et al., 2020). Moreover, cloud scavenging influences the vertical distribution of BC in the atmosphere, with convective precipitation controlling the concentration of BC in the upper troposphere and stratiform precipitation controlling the concentration of BC at the surface (Mahmood et al., 2016). However, the complexity of in-cloud and below-cloud scavenging

of BC limits the ability of global models to reproduce temporal, vertical and horizontal distribution of BC in the whole Arctic region (Whaley et al., 2022) and consequently, BC radiative forcing (Samset et al., 2013, 2018).

65 The ability of BC particles to promote droplet formation (hygroscopicity) is one of the most complex parametrisations in global model schemes. In fact, the cloud nucleation ability of BC depends on fundamental particle properties such as diameter and mixing state, which change during atmospheric ageing due to condensation and coagulation processes. While fresh BC particles are not hygroscopic, aged BC particles show an increase of hygroscopicity (Schwarz et al., 2015; Ohata et al., 2016) connected with the particle diameter (Motos et al., 2019a) and with the formation of inorganic and organic coatings (Dalirian et al., 2018; Motos et al., 2019b). If considerable progresses have been made on the quantification of BC hygroscopicity, its

70 ability to act as an ice nucleating particle is more uncertain. Despite the lac of observations, field and laboratory studies tend to classify BC as a non-efficient ice nucleating particle at least at warm temperatures (Kupiszewski et al., 2016; Kanji et al., 2020).

The study of cloud scavenging of aerosol and BC particles in liquid and mixed-phase clouds becomes additionally complicated by Arctic relevant processes. If nucleation scavenging of aerosol particles from the below-cloud layer might represent the

75 dominant activation mechanism in the Alaskan Arctic (Earle et al., 2011; McFarquhar et al., 2011), Igel et al. (2017) showed that free-tropospheric aerosol particles might be activated at the top of low-level Arctic clouds protruding into the inversion layer (clouds within inversion; Sedlar et al., 2011). This mechanism was suggested to cause downward vertical transport of free-tropospheric aerosol into the boundary layer. Moreover, other in-cloud processes might compete with nucleation scavenging. In fact, interstitial BC particles (BC particles present in the cloud volume but not activated into cloud particles)

80 can be efficiently captured by pre-existing cloud particles via interstitial scavenging (Baumgardner et al., 2008). Despite being often ignored, the number concentration of Arctic aerosol is highly sensitive to interstitial scavenging occurring during long-range transport (Croft et al., 2016). An additional level of complexity is added by cloud processes such as droplet coalescence, riming and Wegener–Bergeron–Findeisen (WBF) process. Without going into details, these processes might modify the size (droplet coalescence and riming) and the phase partitioning (riming: from liquid to ice; WBF: from liquid to interstitial) of

85 activated aerosol (Ding et al., 2019). The understanding of the complex interaction between black carbon and clouds in the Arctic is furthermore complicated by the rarity of in-situ observations, especially at cloud level (Tørseth et al., 2019).

In this work, we will present unprecedented vertically resolved airborne measurements of black carbon particles sampled inside and outside clouds in the European Arctic in summer 2017 during the Arctic CLoud Observations Using airborne measurements during polar Day (ACLOUD) campaign (Wendisch et al., 2018, 2022). The objective is to provide first insights

90 on the BC-cloud interaction in the Arctic with particular focus on: 1) presence and properties of cloud-active BC particles; 2) scavenging mechanisms; 3) impact of cloud processing on BC vertical distribution.

2   Methodology

The ACLOUD campaign was conducted between 23 May and 26 June 2017 in the north west region of Svalbard (Norway) within the framework of the "Arctic Amplification: Climate Relevant Atmospheric and Surface Processes, and Feedback Mechanisms (AC)3" project (Wendisch et al., 2018, 2022), see https://www.ac3-tr.de/. All validated data are published in the World Data Center PANGAEA as instrument-separated data subsets (Ehrlich et al., 2019b, https://doi.org/10.1594/PANGAEA.902603). Flight operations and atmospheric measurements used in this specific work are described in the following, while instrumentation, measured parameters and relative abbreviations are listed in Table 1.

2.1   Flight operations

Atmospheric observations were carried out with two research aircrafts of the Alfred Wegener Institute (AWI), Polar 5 and Polar 6 (Wesche et al., 2016). Polar 5 was equipped with remote-sensing instruments, while Polar 6 was equipped with in-situ measurements. A full list of the deployed instrumentation can be found in Ehrlich et al. (2019). In this work, we will present the results obtained from three subsets of whole 22 research flights. The first subset included 12 flights performed on board of Polar 6 providing the most complete vertical coverage of aerosol and cloud particles up to and altitude of 3500 m asl. The flights were performed on 27 May and on 02, 04, 05, 08, 13, 14, 16, 17, 18, 23, 26 June over open water, marginal sea ice zone, and ground (Figure 1a). The second subset was composed by 4 flights performed on 02, 04, 05, 08 June with repeated sampling of low-level clouds over the marginal sea ice zone (Figure 1b), thus providing the best opportunity to investigate the interaction of black carbon with mixed-phase clouds in the boundary layer. The last subset was composed by one single flight of Polar 6, performed on 25 June, which provided the sole case of clear-sky conditions (Figure 1b).

2.2   Techniques

2.2.1   Meteorological measurements

Meteorological parameters such as pressure, humidity and temperature were recorded at 1 Hz resolution with the basic meteorological sensor suite of Polar 6 fully described in previous works (Herber et al., 2012; Schulz et al., 2019; Ehrlich et al., 2019). T and RH data were merged with aircraft position and air pressure into a 1 Hz basic meteorological dataset (https://doi.org/10.1594/PANGAEA.902849; Hartmann et al., 2019). The potential temperature (T_P) was calculated from measured ambient temperature (T) and ambient pressure (P) as: $T_P = T (P_0/P)^{0.286}$.

2.2.2   Cloud particle measurements

The Small Ice Detector Mark 3 (SID-3; Hirst et al., 2001; Vochezer et al., 2016) allows deriving the cloud particle number size distribution in the 5 - 45 µm diameter range (https://doi.org/10.1594/PANGAEA.900261; Schnaiter and Järvinen, 2019b). Liquid droplets and ice crystals were distinguished based on analysing the SID-3 two-dimensional (2-D) scattering patterns for the particle sphericity as described in Vochezer et al. (2016). A more detailed description of processing the SID-3 data for

ACLOUD including correction of coincidence artefacts can be found in Järvinen et al. (2023). Based on the phase discrimination, we calculated the number concentration (N_{Dro}) of liquid droplets, while the liquid water content (LWC) was calculated from the size distribution assuming spherical particles and a particle density of 1 g cm^{-3}.

125 The Cloud Imaging Probe (CIP, DMT, Longmont, CO, USA; Baumgardner et al., 2001) allows quantifying the dimension and shape of cloud particles and was used to derive the number concentration of non-spherical ice crystals (N_{Ice}; calculated according to circularity as in Crosier et al. (2011) and the ice water content (IWC; calculated with the mass-diameter relationship defined by Brown and Francis 1995). The number size distribution of ice crystals presented in this work is based on effective equivalent diameter, which is more comparable with previous Arctic measurements (Mioche et al., 2017). Due to

130 the large uncertainties in the probe's sensitive area for the smallest particle sizes, the nominal detection size range was reduced in the present work to 75 - 1550 µm. The mass fraction of ice water (IWF) was estimated from the IWC measured by the CIP and the LWC measured by the SID-3. All ice crystals variables derived from CIP measurements are published in the PANGAEA database (https://doi.org/10.1594/PANGAEA.899074; Dupuy et al., 2019).

The Airborne Mobile Aerosol Lidar (AMALi) system installed on board of Polar 5 was used to derive the cloud top height.

135 Previous works provide technical details on the operation principle (Stachlewska, 2005), data processing (Stachlewska et al., 2010) and Arctic deployment (Nakoudi et al., 2020). Cloud top height with a 10 seconds time resolution are available on PANGAEA database (https: //doi.org/10.1594/PANGAEA.899962; Neuber et al., 2019). We will solely discuss the cloud top height data acquired during collocated flights of Polar 5 with Polar 6 occurred on 27-29 June and 02-05-08-13-17 June.

2.2.3   Aerosol particle measurements

140 All aerosol particle data presented in this work were acquired with online single-particle instruments. A Single-Particle Soot Photometer (SP2, version D with 8-channels) by Droplet Measurement Technologies (DMT, Longmont, CO, USA) was used to detect refractory black carbon particles (rBC), following the terminology defined by Petzold et al. (2013). While a brief description of the operating principles of the SP2 and assumptions used in this study is given in the following, comprehensive description of calibration standards and procedure is given by Schwarz et al. (2006), Moteki and Kondo (2010), Gysel et al.

145 (2011) and Laborde et al. (2012). By laser-induced incandescence, the SP2 is capable of quantifying the mass of absorbing and refractory material contained in aerosol particles passing through the high-intensity continuous-wave, intra-cavity laser beam at a wavelength of 1064 nm (Stephens et al., 2003). The incandescence light detector was calibrated with a fullerene soot standard from Alfa Aesar (stock no. 40971, lot no. FS12S011), size selected with a differential mobility analyser (SMPS; TSI, Shoreview, MN, USA). The SP2 installed on the Polar 6 provided the number concentration (N_{rBC}), mass concentration

150 (M_{rBC}) and size distribution of rBC particles in the 0.37 - 178 fg mass range, converted to a mass-equivalent diameter (D_{rBC}) range of 73 - 575 nm using a fixed bulk (void-free) density of 1800 kg m^{-3} (Moteki et al., 2010). The rBC particles associated with a saturated incandesce signal were included in the largest bin of the size distribution (468 nm $< D_{rBC} \leq$ 575 nm) and attributed with the maximum quantifiable mass-equivalent diameter (575 nm) and mass (178 fg).

The geometric mean diameter and modal diameter of the mass size distribution will be abbreviated as $D_{\text{rBC-Geo}}$ and $D_{\text{rBC-Mod}}$, respectively. Previous works estimated the rBC concentration below the SP2's detection limit by fitting the measured size distribution with a lognormal function (e.g. Laborde et al., 2013; Zanatta et al., 2018). This correction was not applied to the ACLOUD data since a clear peak in the number size distribution was rarely resolved and the mass size distribution often culminated at the SP2's upper quantification limit. Previous studies showed that the SP2 is sensitive to metal containing particles such as hematite and magnetite, which might lead to an overestimation of rBC particle concentration (Schwarz et al., 2006; Yoshida et al., 2016). These particles are characterized by lower boiling point and colour ratio (the ratio of thermal emission in the blue and red spectrum) but also by slow heating rate in the laser beam of the SP2. During ACLOUD, particles associated with slow rise-time of the incandesce signal were removed. The colour ratio analysis did not show any clear evidence of the presence of non-rBC yet incandescing particles. The optical diameter of rBC-free particles was inferred from the scattering signal acquired by avalanche photodetectors in the given solid angles under the assumption of spherical particles and a refractive index of 1.50+0i with Mie theory (Bohren and Huffman, 1998). Calibration of the scattering cross section measurements was done using monodisperse spherical polystyrene latex (Thermo Scientific). The leading-edge only technique was applied to estimate the coating thickness of rBC containing particles from the optical diameter of unperturbed rBC cores and rBC-containing particles (Gao et al., 2007). The refractive index of the coating was assumed to be equal to BC-free particles (1.50 + 0i) while the refractive index of rBC cores was set to be 1.90+0.8i. This value, being lower than previous Arctic studies (2.26 + 1.26i; Raatikainen et al., 2015; Kodros et al., 2018; Zanatta et al., 2018) and higher than measurements in continental Europe (1.75 + 0.43i; Yuan et al., 2021), allowed the mass equivalent diameter of rBC core to match its optical diameter. The coating thickness was quantified for rBC particles having a D_{rBC} between 200 nm and 250 nm. It must be noted that the scattering detector failed on 03 June 2017; hence no LEO-fit analysis was performed on the following flights. rBC data acquired with the SP2 are publicly available at https://doi.pangaea.de/10.1594/PANGAEA.899937 (Zanatta and Herber, 2019b).

The Ultra High Sensitivity Aerosol Spectrometer (UHSAS; DMT, Longmont, CO, USA) measured the number concentration (N_{AP}) and size distribution of aerosol particles in the optical diameters range of 60-1000 nm (Cai et al., 2008). The UHSAS was connected in parallel to SP2 at tubing length distance of 15 cm. Due to low signal-to-noise ratio at small sizes, the concentration and size distribution estimated from the UHSAS are valid within the optical diameter range of 80-1000 nm (Zanatta et al., 2020). It must be noted that rapid change of pressure might affect the sample flow measurement and, consequently, the quantification of aerosol particle number concentration by the UHSAS (Brock et al., 2011). Although modification of the UHSAS flow system are recommended for airborne operation (Kupc et al., 2018), Schulz et al. (2019) showed no measuring bias of unmodified UHSAS during low-speed flights installed in the unpressurized cabin of Polar 6. Aerosol particles data acquired with the UHSAS are publicly available at https://doi.pangaea.de/10.1594/PANGAEA.900341 (Zanatta and Herber, 2019a).

2.3 Cloud and aerosol particles sampling

Two different inlets were installed on the front top of the aircraft Polar 6, ahead of the engines to sample the total aerosol and cloud particle residuals. A comprehensive description of the two inlets is given by Ehrlich et al. (2019).

The total aerosol inlet was a stainless-steel inlet with a shrouded diffuser already installed on Polar 6 in previous Arctic campaigns (Leaitch et al., 2016; Schulz et al., 2019). The manifold exhaust flowed freely into the back of the cabin, such that the intake flow varied with the true airspeed of the aircraft. Sampling speed at the inlet tip was approximately isokinetic for the airspeeds during ACLOUD, leading to a near-unity transmission of submicrometric aerosol particles (Ehrlich et al., 2019). A counterflow virtual impactor (CVI; Ogren et al., 1985; Noone et al., 1988) allowed size selective sampling of cloud particles by use of a counterflow at the inlet tip. Depending on the velocity of the particles inside the inlet and the flow rate of the counterflow, smaller cloud and aerosol particles may be decelerated, stopped, and blown out of the inlet. Due to the rather low velocity of the Polar 6, only cloud particles larger 10 µm could be sampled inside clouds by the CVI, while interstitial aerosol and gases and smaller droplets were pre-segregated. Cloud residual particles were then released following evaporation or sublimation of liquid droplets or ice crystals, respectively. Hence, cloud particle residuals were representative of cloud condensation nuclei and/or ice nucleating particles (Mertes et al., 2005, 2007). In order to calculate the concentration of cloud particle residuals, the enrichment factor (EF) needed to be considered. EF was calculated as the ratio between the air volume flows in front and within the CVI, which varied between a minimum of 3.2 and maximum of 5.4 with a median value of 4.2. The transmission efficiency (TE) within the CVI inlet was calculated, similar to Schroder et al. (2015), as the ratio of the number of droplets larger than CVI size cut-off (10 µm; N_{Dro-10}), measured by the SID-3 over the number concentration of aerosol particles measured by the UHSAS in the optical diameter range of 80-1000 nm and corrected by the enrichment factor of CVI. Overall, TE varied between a flight average minimum of 16% (05 June) to a maximum of 23% (on 08 June), with an overall median value of 21%. Finally, the number concentration of rBC in cloud particle residuals ($N_{rBC-res}$) was calculated as:

$$N_{rBC-res} = \frac{N_{rBC}}{EF \times TE}$$

SP2 and UHSAS were operated in parallel and shared a sampling line which was alternatively connected to the total inlet or the CVI inlet. Outside cloud ($N_{Dro} = 0$ cm^{-3} and LWC $= 0$ g m^{-3}), SP2 and UHSAS measurements were performed at the total inlet. Inside cloud ($N_{Dro} \geq 1$ cm^{-3} and LWC ≥ 0.01 g m^{-3}), the SP2 and UHSAS were sampling throughout the CVI inlet line.

3 Results

3.1 Overview of vertical distribution of rBC particles during ACLOUD

Twelve ACLOUD flights were selected to investigate the vertical profile of rBC and cloud particles over the marginal sea ice zone, open water and land in the north-west of Svalbard (Figure 1a). These measurements covered the three synoptic conditions identified during the ACLOUD campaign (Knudsen et al., 2018). One flight (27 May) was performed during the "cold period"

when cold and dry conditions were dominant, four flights (02, 04, 05, 08 June) were performed during the "warm period" in presence of moist air, while seven flights (13, 14, 16, 17, 18, 23, 26 June) were affected by a mixture of air masses, "normal period".

The vertical variability of rBC mass concentration (M_{rBC}) and mass size distribution is shown in Figure 2a and Figure 2b, respectively. For this specific analysis, the in-cloud measurement periods were excluded. Over all altitudes, the median M_{rBC} was 2.3 ng m^{-3} with interquartile range of 0.86-4.8 ng m^{-3}. This low concentration is expected during summer across the full Arctic (Schwarz et al., 2013; Roiger et al., 2015; Schulz et al., 2019) and is connected with limited south-north circulation of airmasses (Bozem et al., 2019) and efficient wet removal south of the polar dome (Croft et al., 2016). Although the impact of pollution plumes is not infrequent in the free-troposphere in the summer Arctic (Roiger et al., 2015), the average vertical profile of M_{rBC} did not show any relevant pollution plume above 500 m asl, where M_{rBC} median concentration varied between 1.7 ng m^{-3} and 3.9 ng m^{-3}. On the contrary, M_{rBC} showed a marked decrease below 500 m asl down to less than 1 ng m^{-3}. Similar to the mass concentration, the mass size distribution of rBC remained relatively stable above 500 m (geometric mean of the mass size distribution between 180 nm and 190) but showed an increasing concentration of larger rBC particles in the lowermost atmospheric layers, where the geometric mean of the mass size distribution was 220 - 250 nm. While the diameter of rBC particles was reported to slightly decrease with altitude in summer in various Arctic regions (Jurányi et al., 2023), the presence of large rBC particles in the lowest atmospheric layer is unusual for summer conditions (Arctic Ocean; Taketani et al., 2016). These larger particles (mass geometric mean diameter above 400 nm) accounted for less than 5% of the total number concentration along the full altitude range. Nonetheless, they represented 37% of the total rBC mass observed in the lowest 500 m asl, and 17% in atmospheric layers aloft. No evident change in mass concentration and size distribution was observed between the cold, warm and normal periods. During ACLOUD, cloud cover exceeded 70%, with a preponderant occurrence of low-level clouds (Wendisch et al., 2018). The presence of low-level clouds was confirmed by collocated remote sensing measurements of the cloud-top height performed on board of the Polar 5 aircraft with the AMALI lidar. The resulting vertical distribution of cloud top height frequency (Figure 2c) showed that 40% of the total clouds were observed below 500 m asl. Due to the variation of BC properties in correspondence of cloud layers in the lowest 500 m of altitude; in the following, we investigate the relationship between black carbon properties and low-level clouds to understand the potential impact of cloud processing on the vertical variability of BC properties in the summer Arctic boundary layer.

3.2   Identification and characterization of low-level clouds

Within this "warm period" of the ACLOUD campaign, four consecutive flights (02 June, 04 June, 05 June and 08 June), conducted north-west of Svalbard between approximately 80°N and 82°N (Figure 1b), allowed investigating the variability of rBC particles above-cloud and below-cloud layers and the properties of rBC residuals. A full description of the atmospheric structure, vertical distribution of cloud particles and vertical coverage of flights operation is given in the supplementary material and is shown Figure S1. The vertical profile of the potential temperature (Figure S1a) suggested that clouds were coupled with the surface (Gierens et al., 2020) and were protruding into the inversion layer but not above inversion top, hence

classified as "cloud inside inversion" (Sedlar et al., 2011). In this relatively warm (temperature interquartile range of IQR -5.8
- -3.9°C) and moist boundary layer (RH > 80%; Figure S1b), liquid droplets dominated the cloud water content (Figure S1c), while ice phase was observed throughout the cloud and precipitation was detected below the cloud (Figure S1d). The cloud events discussed here show many features common to Arctic persistent mixed-phase clouds as summarized by Sedlar et al. (2011), Morrison et al. (2012) and Korolev et al. (2017): dominance of supercooled droplets, intruding-inversion clouds but coupled with the surface and ice sedimentation below-cloud. We can thus conclude that the selected ACLOUD cloud cases fairly represented summer Arctic conditions. Valid cloud residual measurements were performed from 60 m to 544 m asl (cloud thickness of 310 - 435 m). Above-cloud observations performed above inversion top (400 - 750 m asl) are considered to be representative of free-tropospheric conditions, while below-cloud observations (60 - 150 m asl) are considered to be representative of Arctic boundary layer impacted cloud presence. The vertical extent of valid above-cloud, in-cloud and below-cloud measurements of rBC particles and residuals is shown in Figure S1e. The measurement time above cloud, inside and below cloud was of 82, 199 and 84 minutes, respectively. Dominant clear sky conditions were only observed on 25 June (normal-period) over sea ice north of Svalbard (Figure 1b), where no cloud droplets nor ice crystals were observed above and below inversion.

3.3   rBC properties in a cloud-dominated boundary layer

To understand if cloud presence might affect the properties of rBC particles in the boundary layer, we will present the variability of concentration and size distribution of rBC particles from above-cloud to below-cloud for the cloud events observed between 02 and 08 June, and from above inversion to below inversion for the clear sky event on 25 June.

The flight ensemble median rBC mass concentration decreased by a factor of 4 from above-cloud condition (median M_{rBC}=5.5 ng m^{-3}) to below-cloud condition (median M_{rBC}=1.3 ng m^{-3}) for the flights occurred between 02 June and 08 June. The reduction of M_{rBC} from free troposphere to boundary layer observed between 02 June and 08 June reflects the overall vertical profile of rBC mass showed in Figure 2, and might be caused by atmospheric stratification favouring long range transport into the free-troposphere (Croft et al., 2016), inefficient atmospheric mixing between the boundary layer and the free-troposphere (Kupiszewski et al., 2013), and by cloud and sub-cloud wet removal in the boundary layer (Gogoi et al., 2018).

The mass size distribution of rBC above-cloud remained fairly constant for all considered events, and characterized by an overall geometric mean diameter ($D_{rBC-Geo}$) of 192 nm and a modal diameter ($D_{rBC-Mod}$) of 178 nm. Similar values were observed in the free troposphere under clear-sky condition on 25 June ($D_{rBC-Mod}$ = 183 nm, $D_{rBC-Geo}$ = 190 nm; Figure 3d). The steady state of rBC size distribution from the warm-period (02-08 June) to the normal-period (25 June) indicated the presence of homogeneous rBC population in the free troposphere which appeared to be completely independent from cloud presence below inversion-top. The size distribution of rBC aerosol below-cloud was characterized by a $D_{rBC-Mod}$ of 193 nm and a $D_{rBC-Geo}$ of 255 nm, and was enriched in larger rBC particles otherwise not observed in the free troposphere. (Figure 3b). Compared to above-cloud, and increase of rBC particles larger than saturation-diameter (575 nm) was observed below-cloud. These larger particles represented less than 5% of M_{rBC} above-cloud, and 36% of M_{rBC} below-cloud. The rBC size distribution observed in

clear-sky conditions (25 June) within the boundary layer did not show a clear mode in the SP2 size detection range, being depleted in particles larger than 150 - 200 nm (Figure 3d). If the size distribution of free-tropospheric rBC observed during ACLOUD is not uncommon in the Arctic spring and summer, none of previous Arctic studies ever reported rBC size distributions similar to below-cloud conditions, neither in the boundary layer nor in the free troposphere in summer or spring (Raatikainen et al., 2015; Taketani et al., 2016; Kodros et al., 2018; Zanatta et al., 2018; Schulz et al., 2019; Ohata et al., 2021). All told, these results confirmed the general vertical variability presented in Section 3.1, clearly showing that ground observations are not representative of the free troposphere. Moreover, the recurring enhancement of larger rBC particles observed below-cloud compared to above-cloud and its depletion in a clear-sky boundary layer might indicate the influence of cloud processing on rBC properties.

3.4   rBC scavenging processes

The number concentration of rBC particles measured behind the CVI inlet in cloud was low, with median $N_{\text{rBC-res}}$ of 0.58 cm^{-3} and interquartile range of 0.29 - 1.0 cm^{-3}. As a result, only a minor number of cloud droplets contained an rBC particle. The $N_{\text{rBC-res}}/N_{\text{Dro10}}$ ratio ranged from a maximum median of 1.5% on 02 June to a minimum median of 0.69% on 04 June, with a cloud ensemble median of 0.90% and interquartile range of 0.46 - 1.4% (Figure 4a). These results clearly indicated that rBC particles were a minority of cloud active aerosol particles. Considering that the number size distribution culminated at the low quantification limit of the SP2, $N_{\text{rBC-res}}$ and $N_{\text{rBC-res}}/N_{\text{Dro10}}$ were most certainly underestimated. To assess the activation mechanism of rBC particles, we compared the absolute and relative concentration of rBC residuals with rBC particles sampled outside cloud.

3.4.1   Below-cloud nucleation scavenging

Earle et al. (2011) and McFarquhar et al. (2011) fund that the totality of below-cloud aerosol particles was activated in-cloud in the Alaskan Arctic. Following their approach, we calculated the ratio between $N_{\text{rBC-res}}$ over N_{rBC} measured below-cloud ($N_{\text{rBC-blw}}$) and above-cloud ($N_{\text{rBC-abv}}$). $N_{\text{rBC-res}}/N_{\text{rBC-abv}}$ varied from the highest median value of 0.44 on 02 June to the lowest median value of 0.25 on 08 June, with a cloud ensemble median of 0.30 (IQR=0.18-0.47; Figure 4b). The $N_{\text{rBC-res}}/N_{\text{rBC-blw}}$ median values were surprisingly high, ranging from a minimum of 1.05 on 02 June and a maximum of 1.33 on 04 June, with a cloud ensemble median of 1.16 and interquartile range of 0.71-1.76 (Figure 4c). Although the above unity values of $N_{\text{rBC-res}}/N_{\text{rBC-blw}}$ suggested that the totality of rBC particles below-cloud could be activated in cloud via adiabatic lifting (Earle et al., 2011; McFarquhar et al., 2011), the contribution of measurement uncertainty must be considered. The uncertainty of $N_{\text{rBC-res}}$ has multiple contributions: the 1σ reproducibility of N_{rBC} measured by SP2 (5%; Laborde et al., 2012), and the uncertainty associated with the transmission efficiency factor (13%). The latter was estimated by propagating the 1σ reproducibility associated with N_{AP} measured by the UHSAS (9%; Ehrlich et al., 2019) and the uncertainty of N_{Dro} measured by the SID-3 (10%; Baumgardner et al., 2017). The overall uncertainty of $N_{\text{rBC-res}}/N_{\text{rBC-blw}}$ (± 15%) might thus contribute to the $N_{\text{rBC-}}$

blw up to 1.15. Moreover, the sedimentation of ice crystals observed below-cloud (Figure S1d) might reduce $N_{rBC-blw}$ by impaction scavenging (Hegg et al., 2011; Gogoi et al., 2018), hence contributing to the enhanced $N_{rBC-res}/N_{rBC-blw}$ values.

3.4.2   Interstitial and cloud-top scavenging

Other activation mechanisms might occur and contribute to the $N_{rBC-res}/N_{rBC-blw}$ values above unity. First, interstitial aerosol particles may be scavenged via impaction with existing droplets (Croft et al., 2016), potentially enriching the number concentration of rBC-residuals (Baumgardner et al., 2008). We thus compared the fraction of rBC particles measured outside clouds ($F_{rBC} = N_{rBC}/N_{AP}$) and inside clouds ($F_{rBC-res} = N_{rBC-res}/N_{AP-res}$). An increase of $F_{rBC-res}$ compared to outside cloud, might indicate interstitial impaction as the preponderant scavenging mechanism of rBC particles (Baumgardner et al., 2008). During the ACLOUD cases, we found slightly smaller $F_{rBC-res}$ (1.0%) than F_{rBC} above-cloud (2.3%) and below-cloud (1.2%). Similar $F_{rBC-res}$ and F_{rBC} below-cloud suggested that rBC was activated via the same pathway of the bulk aerosol, that rBC and other aerosol particles shared similar hygroscopicity, and that rBC particles were not entering, preferentially, the cloud phase by interstitial scavenging. Second, Igel et al. (2017) showed that free-tropospheric aerosol may be scavenged at the top of stratocumulus Arctic clouds protruding through the inversion layer. Considering that the clouds observed between 02 and 08 June extended into the inversion layer (Figure S1a and Figure 6a), the high N_{rBC} observed above-cloud, with respect to below-cloud, represented a non-negligible source of hygroscopic rBC particles which might have contributed to $N_{rBC-res}/N_{rBC-blw}$ values above unity reported above. To better understand the contribution of below-cloud and cloud-top activation processes we further analysed the size distribution and mixing state of rBC-residuals in Section 3.5 and its vertical variability in Section 3.6.

3.5   Characterization of rBC-residual properties

Diameter and mixing state are fundamental properties controlling the ability of aerosol particles to nucleate a liquid droplet (hygroscopicity). Previous studies showed that larger and internally mixed rBC are more hygroscopic (Dalirian et al., 2018; Motos et al., 2019a), and are enriched in the residual phase compared to outside clouds (Motos et al., 2019b). Hence, to assess the nucleation scavenging during ACLOUD, we present the coating thickness and size distribution of rBC residuals and its variation compared to outside cloud conditions. Due to failure of the scattering detector, the quantification of coating thickness was only possible for the flight occurred on 02 June. Considering that the coating thickness was quantified for rBC cores in the 200 - 250 nm diameter range, which represented a small subset of the total detected rBC particles, the results discussed as following are extremely uncertain due to the low counting statistics.

3.5.1   Coating thickness of rBC residuals on 02 June

First it must be noted that the analysis of the coating thickness includes only rBC particles in the 200-250 nm range of mass equivalent diameter. rBC particles in this diameter range were ubiquitously found above-cloud, inside-cloud and below-cloud (Figure 3). The distribution of coating-thickness is presented in Figure S2 in the supplementary material. The thinnest coatings were observed above clouds, where the coating thickness median was 30 nm (IQR = 23 - 48 nm) and median shell-to-core

ratio was 1.51 (IQR = 1.38 - 1.8). The thickest coatings were observed below clouds, where the median coating thickness was 43 nm (IQR = 25 - 58 nm), and median shell-to-core diameter ratio was 1.67 (IQR = 1.43 - 1.98). The rBC cloud residuals showed medium coating thickness (median = 38 nm, IQR = 25 - 59 nm) and shell-to-core ratio (median = 1.58, IQR = 1.39 – 1.92 nm) respect to above-cloud and coatings to below-cloud. The coating thickness values presented here are similar to previous Arctic ground (Raatikainen et al., 2015; Zanatta et al., 2018) and airborne (Kodros et al., 2018; Ohata et al., 2021) observation, and are substantially higher than urban observations (Laborde et al., 2013; Yoshida et al., 2020). Even though thicker coatings can be found in aged continental air masses, the presence of 30-40 nm thick coatings is sufficient to significantly increase the hygroscopicity of otherwise hydrophobic uncoated BC particles in laboratory experiments (Dalirian et al., 2018) and filed observations (Motos et al., 2019a). Keeping in mind the low counting statistics of the coating analysis, we can conclude that rBC particles sampled during ACLOUD were presentative of aged and hygroscopic rBC particles which could be efficiently activated via nucleation scavenging. However, the reduced temporal coverage and the uncertainty of coating thickness quantification (17%; Laborde et al., 2012) did not allow identifying a significant change in the degree of internal mixing between rBC residuals and rBC particles sampled outside cloud.

3.5.2 Size distribution of rBC residuals

The mass size distribution of rBC residuals was similar during all cloud cases (Figure 3c), indicating similar conditions along the measuring period. A mode at 193 nm was evident in the rBC residuals size distribution, being comparable to rBC particles observed above and below cloud. rBC residuals showed a prominent shoulder towards larger diameters, culminating in the overflow saturation bin (rBC cores larger than 575 nm of mass-equivalent diameter, representing 28% of the $M_{rBC-res}$). This feature was shared only with rBC particles sampled below-cloud. The almost bimodal distribution observed inside-cloud and below-cloud suggested the occurrence of different cloud processes. On one side, the recurring peak around 180-200 nm in the rBC size distribution outside and inside cloud might support the hypothesis of cloud-mediated transport of free-tropospheric rBC in the boundary layer proposed by (Igel et al. (2017). On the other side, the similar size distributions of rBC residuals and rBC particles sampled below-cloud clearly indicate an efficient exchange of rBC particles at the cloud bottom. This exchange might include nucleation from the below-cloud layer (Earle et al., 2011; McFarquhar et al., 2011) followed by release of rBC residuals contained in precipitating droplets below-cloud (Igel et al., 2017). In case of persistent low-level Arctic clouds, this activation and release cycle might occur several times as suggested for ice nucleating particles by Solomon et al. (2015).

To quantify the size-dependent enrichment or depletion of rBC in cloud residuals compared to outside cloud, we calculated the ratio of the number size distribution of rBC residuals over the number size distribution of rBC particles sampled above-cloud and below-cloud. rBC particles were depleted in cloud residuals compared to above-cloud especially in the 80-300 nm D_{rBC} range (Figure 5a). However, rBC particles larger than 400 nm were exponentially enriched in cloud residuals by a 1.5-3.5 factor compared to above-cloud conditions. The ratio of the number size distribution was different for below-cloud rBC (Figure 5b), where the ratio increased from approximately 1 for D_{rBC} below 100 nm to values around 1.5 for D_{rBC} larger than 200 nm. If larger and more hygroscopic rBC particles are usually enriched in cloud residuals (Motos et al., 2019a), Figure 5

shows an absolute enrichment of larger rBC-residuals compared to above-cloud and below-cloud, suggesting that larger rBC-residuals might only exist in the cloud phase and be the result of in-cloud processing.

3.6 Vertical structure of cloud microphysics and rBC residuals

In the following, we addressed the vertical structure of cloud phase and rBC-residuals to better understand the influence of activation from above-cloud and below-cloud, identify any potential cloud processing and their potential effects on rBC residuals properties.

3.6.1 Normalized altitudes

Due to the low counting statistics caused by the low concentration of ice crystals and rBC particles, this analysis is based exclusively on the cloud ensemble. Since cloud top and cloud bottom height showed some variability during the different flight (Figure S1), the vertical variability of cloud and residual properties are presented as function of the in-cloud normalized altitude (Z_n) following Mioche et al. (2017) as:

$$Z_n = \frac{Z - Z_b}{Z_t - Z_b}$$

Where Z is the measurement altitude, Z_b is the lowest altitude of in-cloud valid rBC-residuals measurements and Z_t is highest altitude of in-cloud rBC-residuals measurements. Thus, $Z_n = 1$ and $Z_n = 0$ correspond to the highest and lowest rBC-residuals measurement, respectively. Considering the relatively thin clouds (vertical extent between 310 - 435 m) the cloud was divided into 4 vertical sections (quartiles).

3.6.2 In-cloud vertical profiles

The vertical profile of potential temperature indicated the presence of a homogenous and well-mixed cloud section extending from cloud bottom to $Z_n = 0.75$, where median T_{Pot} values varied within 0.25 K. Increasing T_{Pot} at $Z_n > 0.75$ indicated the cloud intrusion in the inversion layer (Figure 6a). The liquid water content showed an increasing trend from cloud-bottom until $Z_n = 0.75$ where median LWC was 0.27 g m^{-3}, and a decrease in the upper quartile of the cloud ensemble (Figure 6b). The ice water content increased by two orders of magnitude from 1.4×10^{-4} g m^{-3} at cloud top to 1.8×10^{-2} g m^{-3} at cloud bottom (Figure 6c). The number concentration of rBC-residuals increased monotonically from 0.50 cm^{-3} at cloud top to 0.73 cm^{-3} at cloud bottom (Figure 6d). The relative change of $N_{rBC-res}$ between vertically-adjacent quartiles was is in the uncertainty range (14%, see Section 2.2.3), while T-test analysis indicated that the hypothesis of equal $N_{rBC-res}$ averages is confirmed for the two lowermost quartiles ($Z_n < 0.50$), but not for the two uppermost quartiles ($Z_n > 0.5$). Thus, we cannot conclude that the vertical trend (quartile-by-quartile) of $N_{rBC-res}$ is statistically significant. However, cloud top ($Z_n > 0.75$) and cloud bottom ($Z_n < 0.25$) showed a remarkable and statistically significant difference, not only in the number concentration of rBC-residuals, but also in potential temperature and cloud phase. We thus directly compare cloud-top to cloud-bottom.

3.6.3   rBC-residuals properties in a liquid cloud-top and in a mixed-phase cloud-bottom

In the upper quartile of the cloud, while liquid droplets dominated the cloud phase (IWF ~ 0%), only 0.8% of droplets contained an rBC-residual, and the mass size distribution of rBC-residuals showed a dominant peak around 200 nm ($D_{rBC-Mod}$ = 188 nm; Figure 7), similar to above-cloud rBC (Figure 3a). However, a marked tail towards larger diameters was present in the mass size distribution ($D_{rBC-Geo}$ = 231 nm), being more similar to below-cloud conditions (Figure 3b). The rBC-residuals with a mass-equivalent diameter larger than 400 nm accounted for 36% of the total rBC mass at cloud-top. This ratio being closer to below-cloud values (45%) than above-cloud (11%) values. The cloud phase and rBC-residuals properties were different at cloud-bottom. Less and smaller liquid droplets but more and larger ice crystals (Figure S3) lead to an increase of IWF up to 14% at cloud-bottom, where higher $N_{rBC-res}$ was observed (+31%) with respect to cloud-top, and 1.3% of liquid droplets included an rBC-residual. The mass size distribution of rBC-residuals at cloud-bottom was almost identical to cloud-top for D_{rBC} below 200 nm (Figure 7). However, due to the increasing concentration of larger rBC-residuals at cloud-bottom, we did not observe a clear peak in the mass size distribution (as observed at cloud-top, above-cloud, and below-cloud) leading to a $D_{rBC-Geo}$ of 318 nm (+38% compared to cloud-top). Overall, rBC-residuals larger than 400 nm accounted for the majority of the total $M_{rBC-res}$ (62%) at cloud-bottom.

The data presented in this section showed for the first time that the population of rBC residuals in an Arctic cloud is not homogeneous on the vertical scale, indicating that rBC might by scavenged or processed via different pathways, complicating the interpretation of our results. Considering the activation mechanisms, the higher concentration of rBC-residuals at cloud-bottom suggests the predominant activation at cloud-bottom (Earle et al., 2011). However, the increase of T_{Pot} at cloud-top confirmed the intrusion of the cloud into the inversion layer (Sedlar et al., 2011) and reinforces the hypothesis of nucleation scavenging of free-tropospheric rBC at cloud top (Igel et al., 2017), which might contribute to higher concentration of $N_{rBC-res}$ respect to $N_{rBC-blw}$ (Figure 4c). If the preferential nucleation scavenging of larger rBC particles (Motos et al., 2019a, b) might explain the diameter increase inside-cloud respect to outside cloud (Figure 5), cloud processing might also contribute to the metamorphism of rBC-residuals within the cloud. Drizzle droplets, observed during the "warm-period" of ACLOUD (Järvinen et al., 2023), may collect multiple droplets during sedimentation. Hence, few large drizzle droplets may contain multiple rBC-residuals, which might be released as larger rBC-agglomerates after evaporation (Ding et al., 2019). Considering that direct sampling of drizzling drops in the cloud was technically not possible with the CVI inlet installed on the Polar 6, below-cloud release via evaporation (Igel et al., 2017) of rBC-agglomerates and its reactivation at cloud-bottom (Solomon et al., 2015) might contribute to the presence of larger rBC-residuals at cloud-bottom (Figure 7) and explain the similarity between in-cloud and below-cloud size distribution (Figure 3b,c). The increase of IWC at cloud-bottom adds one additional degree of complexity. As shown by Ding et al. (2019), different processes such WBF and riming might modify the phase partitioning and size distribution of rBC residuals in mixed-phase clouds. With our dataset we were, however, unable to confirm nor to exclude the occurrence of liquid and ice driven metamorphism of rBC-residuals.

4   Conclusion

The interaction of black carbon particles with Arctic clouds was investigated with airborne measurements in the north west of Svalbard (Norway) in the framework of the ACLOUD campaign in summer 2017. The overall vertical variability of rBC
440   properties during the ACLOUD campaign indicated a net decrease of rBC concentration and increase of rBC diameter in the lowest atmospheric layer dominated by clouds. Four case events characterized by the presence of low-level, surface-coupled, inside-inversion and mixed-phase clouds were identified.

The analysis of these events confirmed a net separation of rBC properties from the atmospheric layers above-cloud in the free troposphere to the below-cloud layer, where less (median rBC mass concentration of 1.4 ng m^{-3}), larger (geometric mean of
445   the mass size distribution of 251 nm) and more coated (median coating thickness of 43 nm) rBC particles were observed compared to above-cloud conditions (median rBC mass concentration of 5.5 ng m^{-3}, geometric mean of the mass size distribution of 189 nm, and median coating thickness of 30 nm). In the absence of clouds, rBC particles in the boundary layer were dominated by small diameters (geometric mean of the mass size distribution of 147 nm).

Under mixed-phase cloud conditions (median temperature of -5.3°C, median LWC of 0.15 g cm^{-3}, and median IWC of 0.002
450   g cm^{-3}), only a small minority of droplets (less than 1%) contained an rBC particle. It appeared that the totality of rBC particles below the cloud layer was activated, with potential activation of free-tropospheric rBC in the cloud-top extending in the inversion layer. The population of cloud residuals was enriched in larger rBC particles compared to above-cloud conditions (geometric mean of the mass size distribution of 249 nm) very similar to below-cloud rBC. This similarity suggested efficient exchange of rBC particles between the cloud and below-cloud layers. The vertical profiling of the cloud layer showed a clear
455   stratification of rBC-residuals properties from the liquid cloud-top protruding in the inversion layer to the mixed-phase cloud-bottom, potentially suggesting metamorphism of rBC-residuals caused by cloud processing.

To conclude, the ACLOUD observations demonstrated that surface measurements are clearly not representative of the atmosphere aloft. This statement becomes particularly important in presence of low-level mixed-phase, persistent clouds, when recurring cloud processing might influence not only the vertical distribution of black carbon but also its microphysical
460   properties inside-cloud and below-cloud. Considering the short duration of our measurements and the complexity of aerosol-cloud interaction, more observations are needed to constrain activation mechanisms of black carbon and the impacts of cloud processing in the Arctic.

Code and data availability
465   The SP2 data were analysed with PSI Toolkit single particle soot photometer (SP2), version 4.110. Contact Droplet Measurement Technologies to download the software.

Author contributions

The manuscript was written by MZ with contributions from all authors. Cloud particle measurements and subsequent data
470   analysis were performed by OJ, RD, EJ and MS. Aerosol particle measurements and subsequent data analysis were performed
by MZ AH, ZJ, SM, OE and JS. All authors contributed to the data interpretation.

Acknowledgements

The authors thank Christof Lüpkes (Alfred-Wegener-Institut, Helmholtz-Zentrum für Polar- und Meeresforschung (AWI),
475   Bremerhaven, Germany) and Roland Neuber (Alfred-Wegener-Institut, Helmholtz-Zentrum für Polar- und Meeresforschung
(AWI), Potsdam, Germany) for the valuable technical and scientific discussion.

Financial support

We gratefully acknowledge the funding by the Deutsche Forschungsgemeinschaft (DFG, German Research Foundation)–
480   project ID 268020496 – TRR 172, within the Transregional Collaborative Research Center "ArctiC Amplification: Climate
Relevant Atmospheric and SurfaCe Processes, and Feedback Mechanisms (AC)3". Marco Zanatta acknowledges funding by
the Deutsche Forschungsgemeinschaft (DFG, German Research Foundation, grant no. Projektnummer 457895178). Emma
Järvinen acknowledges funding through the Helmholtz Association's Initiative and Networking Fund (grant agreement no.
VH-NG-1531).

References

Baumgardner, D., Jonsson, H., Dawson, W., O'Connor, D., and Newton, R.: The cloud, aerosol and precipitation spectrometer: a new instrument for cloud investigations, Atmospheric Res., 59–60, 251–264, https://doi.org/10.1016/S0169-8095(01)00119-3, 2001.

Baumgardner, D., Subramanian, R., Twohy, C., Stith, J., and Kok, G.: Scavenging of black carbon by ice crystals over the northern Pacific, Geophys. Res. Lett., 35, https://doi.org/10.1029/2008GL035764, 2008.

Baumgardner, D., Abel, S. J., Axisa, D., Cotton, R., Crosier, J., Field, P., Gurganus, C., Heymsfield, A., Korolev, A., Krämer, M., Lawson, P., McFarquhar, G., Ulanowski, Z., and Um, J.: Cloud Ice Properties: In Situ Measurement Challenges, Meteorol. Monogr., 58, 9.1-9.23, https://doi.org/10.1175/AMSMONOGRAPHS-D-16-0011.1, 2017.

Bellouin, N., Quaas, J., Gryspeerdt, E., Kinne, S., Stier, P., Watson-Parris, D., Boucher, O., Carslaw, K. S., Christensen, M., Daniau, A.-L., Dufresne, J.-L., Feingold, G., Fiedler, S., Forster, P., Gettelman, A., Haywood, J. M., Lohmann, U., Malavelle, F., Mauritsen, T., McCoy, D. T., Myhre, G., Mülmenstädt, J., Neubauer, D., Possner, A., Rugenstein, M., Sato, Y., Schulz, M., Schwartz, S. E., Sourdeval, O., Storelvmo, T., Toll, V., Winker, D., and Stevens, B.: Bounding Global Aerosol Radiative Forcing of Climate Change, Rev. Geophys., 58, e2019RG000660, https://doi.org/10.1029/2019RG000660, 2020.

Bohren, C. F. and Huffman, D. R.: Absorption and Scattering of Light by Small Particles, Wiley-VCH Verlag GmbH, Weinheim, Germany, 1998.

Bond, T. C., Streets, D. G., Yarber, K. F., Nelson, S. M., Woo, J.-H., and Klimont, Z.: A technology-based global inventory of black and organic carbon emissions from combustion, J. Geophys. Res. Atmospheres, 109, D14203, https://doi.org/10.1029/2003JD003697, 2004.

Bozem, H., Hoor, P., Kunkel, D., Köllner, F., Schneider, J., Herber, A., Schulz, H., Leaitch, W. R., Aliabadi, A. A., Willis, M. D., Burkart, J., and Abbatt, J. P. D.: Characterization of transport regimes and the polar dome during Arctic spring and summer using in situ aircraft measurements, Atmospheric Chem. Phys., 19, 15049–15071, https://doi.org/10.5194/acp-19-15049-2019, 2019.

Brock, C. A., Cozic, J., Bahreini, R., Froyd, K. D., Middlebrook, A. M., McComiskey, A., Brioude, J., Cooper, O. R., Stohl, A., Aikin, K. C., Gouw, J. A. de, Fahey, D. W., Ferrare, R. A., Gao, R.-S., Gore, W., Holloway, J. S., Hübler, G., Jefferson, A., Lack, D. A., Lance, S., Moore, R. H., Murphy, D. M., Nenes, A., Novelli, P. C., Nowak, J. B., Ogren, J. A., Peischl, J., Pierce, R. B., Pilewskie, P., Quinn, P. K., Ryerson, T. B., Schmidt, K. S., Schwarz, J. P., Sodemann, H., Spackman, J. R., Stark, H., Thomson, D. S., Thornberry, T., Veres, P., Watts, L. A., Warneke, C., and Wollny, A. G.: Characteristics, sources, and transport of aerosols measured in spring 2008 during the aerosol, radiation, and cloud processes affecting Arctic Climate (ARCPAC) Project, Atmospheric Chem. Phys., 11, 2423–2453, https://doi.org/10.5194/acp-11-2423-2011, 2011.

Brooks, I. M., Tjernström, M., Persson, P. O. G., Shupe, M. D., Atkinson, R. A., Canut, G., Birch, C. E., Mauritsen, T., Sedlar, J., and Brooks, B. J.: The Turbulent Structure of the Arctic Summer Boundary Layer During The Arctic Summer Cloud-Ocean Study, J. Geophys. Res. Atmospheres, 122, 9685–9704, https://doi.org/10.1002/2017JD027234, 2017.

Brown, P. R. A. and Francis, P. N.: Improved Measurements of the Ice Water Content in Cirrus Using a Total-Water Probe, J. Atmospheric Ocean. Technol., 12, 410–414, https://doi.org/10.1175/1520-0426(1995)012<0410:IMOTIW>2.0.CO;2, 1995.

520 Cai, Y., Montague, D. C., Mooiweer-Bryan, W., and Deshler, T.: Performance characteristics of the ultra high sensitivity aerosol spectrometer for particles between 55 and 800 nm: Laboratory and field studies, J Aerosol Sci, 39, 759–769, https://doi.org/10.1016/j.jaerosci.2008.04.007, 2008.

Croft, B., Martin, R. V., Leaitch, W. R., Tunved, P., Breider, T. J., D'Andrea, S. D., and Pierce, J. R.: Processes controlling the annual cycle of Arctic aerosol number and size distributions, Atmos Chem Phys, 16, 3665–3682,
525 https://doi.org/10.5194/acp-16-3665-2016, 2016.

Crosier, J., Bower, K. N., Choularton, T. W., Westbrook, C. D., Connolly, P. J., Cui, Z. Q., Crawford, I. P., Capes, G. L., Coe, H., Dorsey, J. R., Williams, P. I., Illingworth, A. J., Gallagher, M. W., and Blyth, A. M.: Observations of ice multiplication in a weakly convective cell embedded in supercooled mid-level stratus, Atmospheric Chem. Phys., 11, 257–273, https://doi.org/10.5194/acp-11-257-2011, 2011.

530 Dalirian, M., Ylisirniö, A., Buchholz, A., Schlesinger, D., Ström, J., Virtanen, A., and Riipinen, I.: Cloud droplet activation of black carbon particles coated with organic compounds of varying solubility, Atmospheric Chem. Phys., 18, 12477–12489, https://doi.org/10.5194/acp-18-12477-2018, 2018.

Ding, S., Zhao, D., He, C., Huang, M., He, H., Tian, P., Liu, Q., Bi, K., Yu, C., Pitt, J., Chen, Y., Ma, X., Chen, Y., Jia, X., Kong, S., Wu, J., Hu, D., Hu, K., Ding, D., and Liu, D.: Observed Interactions Between Black Carbon and Hydrometeor
535 During Wet Scavenging in Mixed-Phase Clouds, Geophys. Res. Lett., 46, 8453–8463, https://doi.org/10.1029/2019GL083171, 2019.

Dou, T.-F. and Xiao, C.-D.: An overview of black carbon deposition and its radiative forcing over the Arctic, Adv. Clim. Change Res., 7, 115–122, https://doi.org/10.1016/j.accre.2016.10.003, 2016.

Dupuy, R., Jourdan, O., Mioche, G., Gourbeyre, C., Leroy, D., and Schwarzenböck, A.: CDP, CIP and PIP In-situ arctic cloud
540 microphysical properties observed during ACLOUD-AC3 campaign in June 2017, https://doi.org/10.1594/PANGAEA.899074, 2019.

Earle, M. E., Liu, P. S. K., Strapp, J. W., Zelenyuk, A., Imre, D., McFarquhar, G. M., Shantz, N. C., and Leaitch, W. R.: Factors influencing the microphysics and radiative properties of liquid-dominated Arctic clouds: Insight from observations of aerosol and clouds during ISDAC, J. Geophys. Res. Atmospheres, 116, https://doi.org/10.1029/2011JD015887, 2011.

545 Ehrlich, A., Wendisch, M., Lüpkes, C., Buschmann, M., Bozem, H., Chechin, D., Clemen, H.-C., Dupuy, R., Eppers, O., Hartmann, J., Herber, A., Jäkel, E., Järvinen, E., Jourdan, O., Kästner, U., Kliesch, L.-L., Köllner, F., Mech, M., Mertes, S., Neuber, R., Ruiz-Donoso, E., Schnaiter, M., Schneider, J., Stapf, J., and Zanatta, M.: A comprehensive in situ and remote sensing data set from the Arctic CLoud Observations Using airborne measurements during polar Day (ACLOUD) campaign, Earth Syst. Sci. Data, 11, 1853–1881, https://doi.org/10.5194/essd-11-1853-2019, 2019.

550 Flanner, M. G.: Arctic climate sensitivity to local black carbon, J. Geophys. Res. Atmospheres, 118, 1840–1851, https://doi.org/10.1002/jgrd.50176, 2013.

Flanner, M. G., Zender, C. S., Hess, P. G., Mahowald, N. M., Painter, T. H., Ramanathan, V., and Rasch, P. J.: Springtime warming and reduced snow cover from carbonaceous particles, Atmos Chem Phys, 9, 2481–2497, https://doi.org/10.5194/acp-9-2481-2009, 2009.

555 Gao, R. S., Schwarz, J. P., Kelly, K. K., Fahey, D. W., Watts, L. A., Thompson, T. L., Spackman, J. R., Slowik, J. G., Cross, E. S., Han, J.-H., Davidovits, P., Onasch, T. B., and Worsnop, D. R.: A Novel Method for Estimating Light-Scattering Properties of Soot Aerosols Using a Modified Single-Particle Soot Photometer, Aerosol Sci. Technol., 41, 125–135, https://doi.org/10.1080/02786820601118398, 2007.

Garrett, T. J., Brattström, S., Sharma, S., Worthy, D. E. J., and Novelli, P.: The role of scavenging in the seasonal transport of
560 black carbon and sulfate to the Arctic, Geophys. Res. Lett., 38, L16805, https://doi.org/10.1029/2011GL048221, 2011.

Gierens, R., Kneifel, S., Shupe, M. D., Ebell, K., Maturilli, M., and Löhnert, U.: Low-level mixed-phase clouds in a complex Arctic environment, Atmospheric Chem. Phys., 20, 3459–3481, https://doi.org/10.5194/acp-20-3459-2020, 2020.

Gogoi, M. M., Babu, S. S., Pandey, S. K., Nair, V. S., Vaishya, A., Girach, I. A., and Koushik, N.: Scavenging ratio of black carbon in the Arctic and the Antarctic, Polar Sci., https://doi.org/10.1016/j.polar.2018.03.002, 2018.

565 Gysel, M., Laborde, M., Olfert, J. S., Subramanian, R., and Gröhn, A. J.: Effective density of Aquadag and fullerene soot black carbon reference materials used for SP2 calibration, Atmos Meas Tech, 4, 2851–2858, https://doi.org/10.5194/amt-4-2851-2011, 2011.

Hartmann, J., Lüpkes, C., and Chechin, D.: 1Hz resolution aircraft measurements of wind and temperature during the ACLOUD campaign in 2017, https://doi.org/10.1594/PANGAEA.902849, 2019.

570 Hegg, D. A., Clarke, A. D., Doherty, S. J., and Ström4, J.: Measurements of black carbon aerosol washout ratio on Svalbard, Tellus B Chem. Phys. Meteorol., 63, 891–900, https://doi.org/10.1111/j.1600-0889.2011.00577.x, 2011.

Herber, A. B., Haas, C., Stone, R. S., Bottenheim, J. W., Liu, P., Li, S.-M., Staebler, R. M., Strapp, J. W., and Dethloff, K.: Regular airborne surveys of Arctic sea ice and atmosphere, Eos Trans. Am. Geophys. Union, 93, 41–42, https://doi.org/10.1029/2012EO040001, 2012.

575 Hirst, E., Kaye, P. H., Greenaway, R. S., Field, P., and Johnson, D. W.: Discrimination of micrometre-sized ice and super-cooled droplets in mixed-phase cloud, Atmos. Environ., 35, 33–47, https://doi.org/10.1016/S1352-2310(00)00377-0, 2001.

Igel, A. L., Ekman, A. M. L., Leck, C., Tjernström, M., Savre, J., and Sedlar, J.: The free troposphere as a potential source of arctic boundary layer aerosol particles, Geophys. Res. Lett., 44, 7053–7060, https://doi.org/10.1002/2017GL073808, 2017.

IPCC, Masson-Delmotte, V., P. Zhai, A. Pirani, S.L., Connors, C. Péan, S. Berger, N. Caud, Y. Chen, L. Goldfarb, M.I. Gomis,
580 M. Huang, K. Leitzell, E. Lonnoy, J.B.R., and Matthews, T.K. Maycock, T. Waterfield, O. Yelekçi, R. Yu, and B. Zhou (eds.): IPCC, 2021: Climate Change 2021: The Physical Science Basis. Contribution of Working Group I to the Sixth Assessment Report of the Intergovernmental Panel on Climate Change, 2021.

Järvinen, E., Nehlert, F., Xu, G., Waitz, F., Mioche, G., Dupuy, R., Jourdan, O., and Schnaiter, M.: Vertical distribution of ice optical and microphysical properties in Arctic low-level mixed-phase clouds during ACLOUD, Clouds and Precipitation/Field
585 Measurements/Troposphere/Physics (physical properties and processes), https://doi.org/10.5194/acp-2022-855, 2023.

Jurányi, Z., Zanatta, M., Lund, M. T., Samset, B. H., Skeie, R. B., Sharma, S., Wendisch, M., and Herber, A.: Atmospheric concentrations of black carbon are substantially higher in spring than summer in the Arctic, Commun. Earth Environ., 4, 1–12, https://doi.org/10.1038/s43247-023-00749-x, 2023.

Kanji, Z. A., Welti, A., Corbin, J. C., and Mensah, A. A.: Black Carbon Particles Do Not Matter for Immersion Mode Ice

590   Nucleation, Geophys. Res. Lett., 47, e2019GL086764, https://doi.org/10.1029/2019GL086764, 2020.

Knudsen, E. M., Heinold, B., Dahlke, S., Bozem, H., Crewell, S., Gorodetskaya, I. V., Heygster, G., Kunkel, D., Maturilli, M., Mech, M., Viceto, C., Rinke, A., Schmithüsen, H., Ehrlich, A., Macke, A., Lüpkes, C., and Wendisch, M.: Meteorological conditions during the ACLOUD/PASCAL field campaign near Svalbard in early summer 2017, Atmospheric Chem. Phys., 18, 17995–18022, https://doi.org/10.5194/acp-18-17995-2018, 2018.

595   Kodros, J. K., Hanna, S. J., Bertram, A. K., Leaitch, W. R., Schulz, H., Herber, A. B., Zanatta, M., Burkart, J., Willis, M. D., Abbatt, J. P. D., and Pierce, J. R.: Size-resolved mixing state of black carbon in the Canadian high Arctic and implications for simulated direct radiative effect, Atmospheric Chem. Phys., 18, 11345–11361, https://doi.org/10.5194/acp-18-11345-2018, 2018.

Korolev, A., McFarquhar, G., Field, P. R., Franklin, C., Lawson, P., Wang, Z., Williams, E., Abel, S. J., Axisa, D., Borrmann,

600   S., Crosier, J., Fugal, J., Krämer, M., Lohmann, U., Schlenczek, O., Schnaiter, M., and Wendisch, M.: Mixed-Phase Clouds: Progress and Challenges, Meteorol. Monogr., 58, 5.1-5.50, https://doi.org/10.1175/AMSMONOGRAPHS-D-17-0001.1, 2017.

Kupc, A., Williamson, C., Wagner, N. L., Richardson, M., and Brock, C. A.: Modification, calibration, and performance of the Ultra-High Sensitivity Aerosol Spectrometer for particle size distribution and volatility measurements during the Atmospheric Tomography Mission (ATom) airborne campaign, Atmospheric Meas. Tech., 11, 369–383,

605   https://doi.org/10.5194/amt-11-369-2018, 2018.

Kupiszewski, P., Leck, C., Tjernström, M., Sjogren, S., Sedlar, J., Graus, M., Müller, M., Brooks, B., Swietlicki, E., Norris, S., and Hansel, A.: Vertical profiling of aerosol particles and trace gases over the central Arctic Ocean during summer, Atmospheric Chem. Phys., 13, 12405–12431, https://doi.org/10.5194/acp-13-12405-2013, 2013.

Kupiszewski, P., Zanatta, M., Mertes, S., Vochezer, P., Lloyd, G., Schneider, J., Schenk, L., Schnaiter, M., Baltensperger, U.,

610   Weingartner, E., and Gysel, M.: Ice residual properties in mixed-phase clouds at the high-alpine Jungfraujoch site, J. Geophys. Res. Atmospheres, 2016JD024894, https://doi.org/10.1002/2016JD024894, 2016.

Laborde, M., Schnaiter, M., Linke, C., Saathoff, H., Naumann, K.-H., Möhler, O., Berlenz, S., Wagner, U., Taylor, J. W., Liu, D., Flynn, M., Allan, J. D., Coe, H., Heimerl, K., Dahlkötter, F., Weinzierl, B., Wollny, A. G., Zanatta, M., Cozic, J., Laj, P., Hitzenberger, R., Schwarz, J. P., and Gysel, M.: Single Particle Soot Photometer intercomparison at the AIDA chamber,

615   Atmospheric Meas. Tech., 5, 3077–3097, https://doi.org/10.5194/amt-5-3077-2012, 2012.

Laborde, M., Crippa, M., Tritscher, T., Jurányi, Z., Decarlo, P. F., Temime-Roussel, B., Marchand, N., Eckhardt, S., Stohl, A., Baltensperger, U., Prévôt, A. S. H., Weingartner, E., and Gysel, M.: Black carbon physical properties and mixing state in the European megacity Paris, Atmos Chem Phys, 13, 5831–5856, https://doi.org/10.5194/acp-13-5831-2013, 2013.

Leaitch, W. R., Korolev, A., Aliabadi, A. A., Burkart, J., Willis, M. D., Abbatt, J. P. D., Bozem, H., Hoor, P., Köllner, F.,
620 Schneider, J., Herber, A., Konrad, C., and Brauner, R.: Effects of 20–100 nm particles on liquid clouds in the cleansummertime Arctic, Atmospheric Chem. Phys., 16, 11107–11124, https://doi.org/10.5194/acp-16-11107-2016, 2016.

Lubin, D. and Vogelmann, A. M.: A climatologically significant aerosol longwave indirect effect in the Arctic, Nature, 439, 453–456, https://doi.org/10.1038/nature04449, 2006.

Mahmood, R., von Salzen, K., Flanner, M., Sand, M., Langner, J., Wang, H., and Huang, L.: Seasonality of global and Arctic
625 black carbon processes in the Arctic Monitoring and Assessment Programme models, J. Geophys. Res. Atmospheres, 2016JD024849, https://doi.org/10.1002/2016JD024849, 2016.

McFarquhar, G. M., Ghan, S., Verlinde, J., Korolev, A., Strapp, J. W., Schmid, B., Tomlinson, J. M., Wolde, M., Brooks, S. D., Cziczo, D., Dubey, M. K., Fan, J., Flynn, C., Gultepe, I., Hubbe, J., Gilles, M. K., Laskin, A., Lawson, P., Leaitch, W. R., Liu, P., Liu, X., Lubin, D., Mazzoleni, C., Macdonald, A.-M., Moffet, R. C., Morrison, H., Ovchinnikov, M., Shupe, M. D.,
630 Turner, D. D., Xie, S., Zelenyuk, A., Bae, K., Freer, M., and Glen, A.: Indirect and Semi-direct Aerosol Campaign: The Impact of Arctic Aerosols on Clouds, Bull. Am. Meteorol. Soc., 92, 183–201, https://doi.org/10.1175/2010BAMS2935.1, 2011.

Mertes, S., Lehmann, K., Nowak, A., Massling, A., and Wiedensohler, A.: Link between aerosol hygroscopic growth and droplet activation observed for hill-capped clouds at connected flow conditions during FEBUKO, Atmos. Environ., 39, 4247–4256, https://doi.org/10.1016/j.atmosenv.2005.02.010, 2005.

635 Mertes, S., Verheggen, B., Walter, S., Connolly, P., Ebert, M., Schneider, J., Bower, K. N., Cozic, J., Weinbruch, S., Baltensperger, U., and Weingartner, E.: Counterflow Virtual Impactor Based Collection of Small Ice Particles in Mixed-Phase Clouds for the Physico-Chemical Characterization of Tropospheric Ice Nuclei: Sampler Description and First Case Study, Aerosol Sci. Technol., 41, 848–864, https://doi.org/10.1080/02786820701501881, 2007.

Mioche, G., Jourdan, O., Delanoë, J., Gourbeyre, C., Febvre, G., Dupuy, R., Monier, M., Szczap, F., Schwarzenboeck, A., and
640 Gayet, J.-F.: Vertical distribution of microphysical properties of Arctic springtime low-level mixed-phase clouds over the Greenland and Norwegian seas, Atmospheric Chem. Phys., 17, 12845–12869, https://doi.org/10.5194/acp-17-12845-2017, 2017.

Mori, T., Kondo, Y., Ohata, S., Zhao, Y., Sinha, P. R., Oshima, N., Matsui, H., Moteki, N., and Koike, M.: Seasonal Variation of Wet Deposition of Black Carbon in Arctic Alaska, J. Geophys. Res. Atmospheres, 125, e2019JD032240,
645 https://doi.org/10.1029/2019JD032240, 2020.

Morrison, H., de Boer, G., Feingold, G., Harrington, J., Shupe, M. D., and Sulia, K.: Resilience of persistent Arctic mixed-phase clouds, Nat. Geosci., 5, 11–17, https://doi.org/10.1038/ngeo1332, 2012.

Moteki, N. and Kondo, Y.: Dependence of Laser-Induced Incandescence on Physical Properties of Black Carbon Aerosols: Measurements and Theoretical Interpretation, Aerosol Sci. Technol., 44, 663–675,
650 https://doi.org/10.1080/02786826.2010.484450, 2010.

Moteki, N., Kondo, Y., and Nakamura, S.: Method to measure refractive indices of small nonspherical particles: Application to black carbon particles, J. Aerosol Sci., 41, 513–521, https://doi.org/10.1016/j.jaerosci.2010.02.013, 2010.

Motos, G., Schmale, J., Corbin, J. C., Modini, R. L., Karlen, N., Bertò, M., Baltensperger, U., and Gysel-Beer, M.: Cloud droplet activation properties and scavenged fraction of black carbon in liquid-phase clouds at the high-alpine research station

655   Jungfraujoch (3580 m a.s.l.), Atmospheric Chem. Phys., 19, 3833–3855, https://doi.org/10.5194/acp-19-3833-2019, 2019a.

Motos, G., Schmale, J., Corbin, J. C., Zanatta, M., Baltensperger, U., and Gysel-Beer, M.: Droplet activation behaviour of atmospheric black carbon particles in fog as a function of their size and mixing state, Atmospheric Chem. Phys., 19, 2183–2207, https://doi.org/10.5194/acp-19-2183-2019, 2019b.

660   Nakoudi, K., Ritter, C., Böckmann, C., Kunkel, D., Eppers, O., Rozanov, V., Mei, L., Pefanis, V., Jäkel, E., Herber, A., Maturilli, M., and Neuber, R.: Does the Intra-Arctic Modification of Long-Range Transported Aerosol Affect the Local Radiative Budget? (A Case Study), Remote Sens., 12, 2112, https://doi.org/10.3390/rs12132112, 2020.

Neuber, R., Schmidt, L. V., Ritter, C., and Mech, M.: Cloud top altitudes observed with airborne lidar during the ACLOUD campaign, https://doi.org/10.1594/PANGAEA.899962, 2019.

665   Noone, K. J., Ogren, J. A., Heintzenberg, J., Charlson, R. J., and Covert, D. S.: Design and Calibration of a Counterflow Virtual Impactor for Sampling of Atmospheric Fog and Cloud Droplets, Aerosol Sci. Technol., 8, 235–244, https://doi.org/10.1080/02786828808959186, 1988.

Ogren, J. A., Heintzenberg, J., and Charlson, R. J.: In-situ sampling of clouds with a droplet to aerosol converter, Geophys Res Lett, 12, 121–124, https://doi.org/10.1029/GL012i003p00121, 1985.

670   Ohata, S., Schwarz, J. P., Moteki, N., Koike, M., Takami, A., and Kondo, Y.: Hygroscopicity of materials internally mixed with black carbon measured in Tokyo, J. Geophys. Res. Atmospheres, 121, 2015JD024153, https://doi.org/10.1002/2015JD024153, 2016.

Ohata, S., Koike, M., Yoshida, A., Moteki, N., Adachi, K., Oshima, N., Matsui, H., Eppers, O., Bozem, H., Zanatta, M., and Herber, A. B.: Arctic black carbon during PAMARCMiP 2018 and previous aircraft experiments in spring, Atmospheric Chem.

675   Phys., 21, 15861–15881, https://doi.org/10.5194/acp-21-15861-2021, 2021.

Oshima, N., Yukimoto, S., Deushi, M., Koshiro, T., Kawai, H., Tanaka, T. Y., and Yoshida, K.: Global and Arctic effective radiative forcing of anthropogenic gases and aerosols in MRI-ESM2.0, Prog. Earth Planet. Sci., 7, 38, https://doi.org/10.1186/s40645-020-00348-w, 2020.

Petzold, A., Onasch, T., Kebabian, P., and Freedman, A.: Intercomparison of a Cavity Attenuated Phase Shift-based extinction

680   monitor (CAPS PMex) with an integrating nephelometer and a filter-based absorption monitor, Atmos Meas Tech, 6, 1141–1151, https://doi.org/10.5194/amt-6-1141-2013, 2013.

Quinn, P. K., Stohl, A., Arnold, S., Baklanov, A., Berntsen, T. K., Christensen, J. H., Eckhardt, S., Flanner, M., Klimont, Z., Korsholm, U. S., and others: AMAP Assessment 2015: Black carbon and ozone as Arctic climate forcers, 2015.

Raatikainen, T., Brus, D., Hyvärinen, A.-P., Svensson, J., Asmi, E., and Lihavainen, H.: Black carbon concentrations and

685   mixing state in the Finnish Arctic, Atmos Chem Phys, 15, 10057–10070, https://doi.org/10.5194/acp-15-10057-2015, 2015.

Roiger, A., Thomas, J.-L., Schlager, H., Law, K. S., Kim, J., Schäfler, A., Weinzierl, B., Dahlkötter, F., Krisch, I., Marelle, L., Minikin, A., Raut, J.-C., Reiter, A., Rose, M., Scheibe, M., Stock, P., Baumann, R., Bouarar, I., Clerbaux, C., George, M., Onishi, T., and Flemming, J.: Quantifying Emerging Local Anthropogenic Emissions in the Arctic Region: The ACCESS Aircraft Campaign Experiment, Bull. Am. Meteorol. Soc., 96, 441–460, https://doi.org/10.1175/BAMS-D-13-00169.1, 2015.

690 Samset, B. H., Myhre, G., Schulz, M., Balkanski, Y., Bauer, S., Berntsen, T. K., Bian, H., Bellouin, N., Diehl, T., Easter, R. C., Ghan, S. J., Iversen, T., Kinne, S., Kirkevåg, A., Lamarque, J.-F., Lin, G., Liu, X., Penner, J. E., Seland, Ø., Skeie, R. B., Stier, P., Takemura, T., Tsigaridis, K., and Zhang, K.: Black carbon vertical profiles strongly affect its radiative forcing uncertainty, Atmos Chem Phys, 13, 2423–2434, https://doi.org/10.5194/acp-13-2423-2013, 2013.

Samset, B. H., Stjern, C. W., Andrews, E., Kahn, R. A., Myhre, G., Schulz, M., and Schuster, G. L.: Aerosol Absorption: 695 Progress Towards Global and Regional Constraints, Curr. Clim. Change Rep., 4, 65–83, https://doi.org/10.1007/s40641-018-0091-4, 2018.

Sand, M., Berntsen, T. K., Kay, J. E., Lamarque, J. F., Seland, Ø., and Kirkevåg, A.: The Arctic response to remote and local forcing of black carbon, Atmos Chem Phys, 13, 211–224, https://doi.org/10.5194/acp-13-211-2013, 2013.

Schnaiter, M. and Järvinen, E.: SID-3 1Hz size distribution of cloud particles during the ACLOUD campaign in 2017, 700 https://doi.org/10.1594/PANGAEA.900261, 2019.

Schroder, J. C., Hanna, S. J., Modini, R. L., Corrigan, A. L., Kreidenwies, S. M., Macdonald, A. M., Noone, K. J., Russell, L. M., Leaitch, W. R., and Bertram, A. K.: Size-resolved observations of refractory black carbon particles in cloud droplets at a marine boundary layer site, Atmos Chem Phys, 15, 1367–1383, https://doi.org/10.5194/acp-15-1367-2015, 2015.

Schulz, H., Zanatta, M., Bozem, H., Leaitch, W. R., Herber, A. B., Burkart, J., Willis, M. D., Kunkel, D., Hoor, P. M., Abbatt, 705 J. P. D., and Gerdes, R.: High Arctic aircraft measurements characterising black carbon vertical variability in spring and summer, Atmospheric Chem. Phys., 19, 2361–2384, https://doi.org/10.5194/acp-19-2361-2019, 2019.

Schwarz, J. P., Gao, R. S., Fahey, D. W., Thomson, D. S., Watts, L. A., Wilson, J. C., Reeves, J. M., Darbeheshti, M., Baumgardner, D. G., Kok, G. L., Chung, S. H., Schulz, M., Hendricks, J., Lauer, A., Kärcher, B., Slowik, J. G., Rosenlof, K. H., Thompson, T. L., Langford, A. O., Loewenstein, M., and Aikin, K. C.: Single-particle measurements of midlatitude black 710 carbon and light-scattering aerosols from the boundary layer to the lower stratosphere, J. Geophys. Res. Atmospheres, 111, D16207, https://doi.org/10.1029/2006JD007076, 2006.

Schwarz, J. P., Samset, B. H., Perring, A. E., Spackman, J. R., Gao, R. S., Stier, P., Schulz, M., Moore, F. L., Ray, E. A., and Fahey, D. W.: Global-scale seasonally resolved black carbon vertical profiles over the Pacific, Geophys. Res. Lett., 40, 2013GL057775, https://doi.org/10.1002/2013GL057775, 2013.

715 Schwarz, J. P., Perring, A. E., Markovic, M. Z., Gao, R. S., Ohata, S., Langridge, J., Law, D., McLaughlin, R., and Fahey, D. W.: Technique and theoretical approach for quantifying the hygroscopicity of black-carbon-containing aerosol using a single particle soot photometer, J. Aerosol Sci., 81, 110–126, https://doi.org/10.1016/j.jaerosci.2014.11.009, 2015.

Sedlar, J., Shupe, M. D., and Tjernström, M.: On the Relationship between Thermodynamic Structure and Cloud Top, and Its Climate Significance in the Arctic, J. Clim., 25, 2374–2393, https://doi.org/10.1175/JCLI-D-11-00186.1, 2011.

720 Shupe, M. D. and Intrieri, J. M.: Cloud Radiative Forcing of the Arctic Surface: The Influence of Cloud Properties, Surface Albedo, and Solar Zenith Angle, J. Clim., 17, 616–628, https://doi.org/10.1175/1520-0442(2004)017<0616:CRFOTA>2.0.CO;2, 2004.

Shupe, M. D., Persson, P. O. G., Brooks, I. M., Tjernström, M., Sedlar, J., Mauritsen, T., Sjogren, S., and Leck, C.: Cloud and boundary layer interactions over the Arctic sea ice in late summer, Atmospheric Chem. Phys., 13, 9379–9399,

725 https://doi.org/10.5194/acp-13-9379-2013, 2013.

Solomon, A., Feingold, G., and Shupe, M. D.: The role of ice nuclei recycling in the maintenance of cloud ice in Arctic mixed-phase stratocumulus, Atmospheric Chem. Phys., 15, 10631–10643, https://doi.org/10.5194/acp-15-10631-2015, 2015.

Stachlewska, I. S.: Investigation of tropospheric arctic aerosol and mixed-phase clouds using airborne lidar technique, Universität Potsdam, 2005.

730 Stachlewska, I. S., Neuber, R., Lampert, A., Ritter, C., and Wehrle, G.: AMALi – the Airborne Mobile Aerosol Lidar for Arctic research, Atmospheric Chem. Phys., 10, 2947–2963, https://doi.org/10.5194/acp-10-2947-2010, 2010.

Stephens, M., Turner, N., and Sandberg, J.: Particle identification by laser-induced incandescence in a solid-state laser cavity, Appl. Opt., 42, 3726–3736, https://doi.org/10.1364/AO.42.003726, 2003.

Taketani, F., Miyakawa, T., Takashima, H., Komazaki, Y., Kanaya, Y., Taketani, F., Miyakawa, T., Inoue, J., Kanaya, Y.,

735 Takashima, H., Pan, X., and Inoue, J.: Ship-borne observations of atmospheric black carbon aerosol particles over the Arctic Ocean, Bering Sea, and North Pacific Ocean during September 2014, J. Geophys. Res. Atmospheres, 2015JD023648, https://doi.org/10.1002/2015JD023648, 2016.

Tørseth, K., Andrews, E., Asmi, E., Eleftheriadis, K., Fiebig, M., Herber, A., Huang, L., Kylling, A., Lupi, A., Massling, A., Mazzola, M., Nøjgaard, J. K., Popovicheva, O., Schichtel, B., Schmale, J., Sharma, S., Skov, H., Stebel, K., Vasel, B., Vitale,

740 V., Whaley, C., Yttri, K. E., and Zanatta, M.: Review of Observation Capacities and Data Availability for Black Carbon in the Arctic Region:EU Action on Black Carbon inthe Arctic – Technical Report 1, 2019.

Vochezer, P., Järvinen, E., Wagner, R., Kupiszewski, P., Leisner, T., and Schnaiter, M.: In situ characterization of mixed phase clouds using the Small Ice Detector and the Particle Phase Discriminator, Atmospheric Meas. Tech., 9, 159–177, https://doi.org/10.5194/amt-9-159-2016, 2016.

745 Wendisch, M., Macke, A., Ehrlich, A., Lüpkes, C., Mech, M., Chechin, D., Dethloff, K., Velasco, C. B., Bozem, H., Brückner, M., Clemen, H.-C., Crewell, S., Donth, T., Dupuy, R., Ebell, K., Egerer, U., Engelmann, R., Engler, C., Eppers, O., Gehrmann, M., Gong, X., Gottschalk, M., Gourbeyre, C., Griesche, H., Hartmann, J., Hartmann, M., Heinold, B., Herber, A., Herrmann, H., Heygster, G., Hoor, P., Jafariserajehlou, S., Jäkel, E., Järvinen, E., Jourdan, O., Kästner, U., Kecorius, S., Knudsen, E. M., Köllner, F., Kretzschmar, J., Lelli, L., Leroy, D., Maturilli, M., Mei, L., Mertes, S., Mioche, G., Neuber, R., Nicolaus, M.,

750 Nomokonova, T., Notholt, J., Palm, M., van Pinxteren, M., Quaas, J., Richter, P., Ruiz-Donoso, E., Schäfer, M., Schmieder, K., Schnaiter, M., Schneider, J., Schwarzenböck, A., Seifert, P., Shupe, M. D., Siebert, H., Spreen, G., Stapf, J., Stratmann, F., Vogl, T., Welti, A., Wex, H., Wiedensohler, A., Zanatta, M., and Zeppenfeld, S.: The Arctic Cloud Puzzle: Using

ACLOUD/PASCAL Multiplatform Observations to Unravel the Role of Clouds and Aerosol Particles in Arctic Amplification, Bull. Am. Meteorol. Soc., 100, 841–871, https://doi.org/10.1175/BAMS-D-18-0072.1, 2018.

755 Wendisch, M., Brückner, M., Crewell, S., Ehrlich, A., Notholt, J., Lüpkes, C., Macke, A., Burrows, J. P., Rinke, A., Quaas, J., Maturilli, M., Schemann, V., Shupe, M. D., Akansu, E. F., Barrientos-Velasco, C., Bärfuss, K., Blechschmidt, A.-M., Block, K., Bougoudis, I., Bozem, H., Böckmann, C., Bracher, A., Bresson, H., Bretschneider, L., Buschmann, M., Chechin, D. G., Chylik, J., Dahlke, S., Deneke, H., Dethloff, K., Donth, T., Dorn, W., Dupuy, R., Ebell, K., Egerer, U., Engelmann, R., Eppers, O., Gerdes, R., Gierens, R., Gorodetskaya, I. V., Gottschalk, M., Griesche, H., Gryanik, V. M., Handorf, D., Harm-Altstädter,

760 B., Hartmann, J., Hartmann, M., Heinold, B., Herber, A., Herrmann, H., Heygster, G., Höschel, I., Hofmann, Z., Hölemann, J., Hünerbein, A., Jafariserajehlou, S., Jäkel, E., Jacobi, C., Janout, M., Jansen, F., Jourdan, O., Jurányi, Z., Kalesse-Los, H., Kanzow, T., Käthner, R., Kliesch, L. L., Klingebiel, M., Knudsen, E. M., Kovács, T., Körtke, W., Krampe, D., Kretzschmar, J., Kreyling, D., Kulla, B., Kunkel, D., Lampert, A., Lauer, M., Lelli, L., Lerber, A. von, Linke, O., Löhnert, U., Lonardi, M., Losa, S. N., Losch, M., Maahn, M., Mech, M., Mei, L., Mertes, S., Metzner, E., Mewes, D., Michaelis, J., Mioche, G., Moser,

765 M., Nakoudi, K., Neggers, R., Neuber, R., Nomokonova, T., Oelker, J., Papakonstantinou-Presvelou, I., et al.: Atmospheric and Surface Processes, and Feedback Mechanisms Determining Arctic Amplification: A Review of First Results and Prospects of the (AC)3 Project, Bull. Am. Meteorol. Soc., 1, https://doi.org/10.1175/BAMS-D-21-0218.1, 2022.

Wesche, C., Steinhage, D., and Nixdorf, U.: Polar aircraft Polar5 and Polar6 operated by the Alfred Wegener Institute, J. Large-Scale Res. Facil. JLSRF, 2, 87, https://doi.org/10.17815/jlsrf-2-153, 2016.

770 Whaley, C. H., Mahmood, R., von Salzen, K., Winter, B., Eckhardt, S., Arnold, S., Beagley, S., Becagli, S., Chien, R.-Y., Christensen, J., Damani, S. M., Dong, X., Eleftheriadis, K., Evangeliou, N., Faluvegi, G., Flanner, M., Fu, J. S., Gauss, M., Giardi, F., Gong, W., Hjorth, J. L., Huang, L., Im, U., Kanaya, Y., Krishnan, S., Klimont, Z., Kühn, T., Langner, J., Law, K. S., Marelle, L., Massling, A., Olivié, D., Onishi, T., Oshima, N., Peng, Y., Plummer, D. A., Popovicheva, O., Pozzoli, L., Raut, J.-C., Sand, M., Saunders, L. N., Schmale, J., Sharma, S., Skeie, R. B., Skov, H., Taketani, F., Thomas, M. A., Traversi, R.,

775 Tsigaridis, K., Tsyro, S., Turnock, S., Vitale, V., Walker, K. A., Wang, M., Watson-Parris, D., and Weiss-Gibbons, T.: Model evaluation of short-lived climate forcers for the Arctic Monitoring and Assessment Programme: a multi-species, multi-model study, Atmospheric Chem. Phys., 22, 5775–5828, https://doi.org/10.5194/acp-22-5775-2022, 2022.

Xu, J.-W., Martin, R. V., Morrow, A., Sharma, S., Huang, L., Leaitch, W. R., Burkart, J., Schulz, H., Zanatta, M., Willis, M. D., Henze, D. K., Lee, C. J., Herber, A. B., and Abbatt, J. P. D.: Source attribution of Arctic black carbon constrained by

780 aircraft and surface measurements, Atmospheric Chem. Phys., 17, 11971–11989, https://doi.org/10.5194/acp-17-11971-2017, 2017.

Yoshida, A., Moteki, N., Ohata, S., Mori, T., Tada, R., Dagsson-Waldhauserová, P., and Kondo, Y.: Detection of light-absorbing iron oxide particles using a modified single-particle soot photometer, Aerosol Sci. Technol., 50, 1–4, https://doi.org/10.1080/02786826.2016.1146402, 2016.

785   Yoshida, A., Moteki, N., Ohata, S., Mori, T., Koike, M., Kondo, Y., Matsui, H., Oshima, N., Takami, A., and Kita, K.: Abundances and Microphysical Properties of Light-Absorbing Iron Oxide and Black Carbon Aerosols Over East Asia and the Arctic, J. Geophys. Res. Atmospheres, 125, e2019JD032301, https://doi.org/10.1029/2019JD032301, 2020.

Yuan, J., Modini, R. L., Zanatta, M., Herber, A. B., Müller, T., Wehner, B., Poulain, L., Tuch, T., Baltensperger, U., and Gysel-Beer, M.: Variability in the mass absorption cross section of black carbon (BC) aerosols is driven by BC internal mixing

790   state at a central European background site (Melpitz, Germany) in winter, Atmospheric Chem. Phys., 21, 635–655, https://doi.org/10.5194/acp-21-635-2021, 2021.

Zanatta, M. and Herber, A.: Aircraft measurements of aerosol size distribution in the Arctic during the ACLOUD campaign 2017, https://doi.org/10.1594/PANGAEA.900341, 2019a.

Zanatta, M. and Herber, A.: Aircraft measurements of refractory black carbon in the Arctic during the ACLOUD campaign

795   2017, https://doi.org/10.1594/PANGAEA.899937, 2019b.

Zanatta, M., Laj, P., Gysel, M., Baltensperger, U., Vratolis, S., Eleftheriadis, K., Kondo, Y., Dubuisson, P., Winiarek, V., Kazadzis, S., Tunved, P., and Jacobi, H.-W.: Effects of mixing state on optical and radiative properties of black carbon in the European Arctic, Atmospheric Chem. Phys., 18, 14037–14057, https://doi.org/10.5194/acp-18-14037-2018, 2018.

Zanatta, M., Bozem, H., Köllner, F., Schneider, J., Kunkel, D., Hoor, P., Faria, J. de, Petzold, A., Bundke, U., Hayden, K.,

800   Staebler, R. M., Schulz, H., and Herber, A. B.: Airborne survey of trace gases and aerosols over the Southern Baltic Sea: from clean marine boundary layer to shipping corridor effect, Tellus B Chem. Phys. Meteorol., 72, 1–24, https://doi.org/10.1080/16000889.2019.1695349, 2020.

Tables

Table 1 List of atmospheric variables observed and computed in this study. Including meteorology, aerosol particle (AP), refectory black carbon particles (rBC) and cloud particles.

Variable	Symbol	Unit	Instrument	Inlet	Aircraft	Size range (diameter)
Meteorology						
Temperature	T	°C	-	-	P6	-
Potential temperature	T_P	°C	-	-	P6	-
Relative humidity	RH	%	-	-	P6	-
Aerosol particle, AP						
AP number concentration	N_{AP}	cm^{-3}	UHSAS	Total	P6	80-1000 nm
AP residuals number concentration	N_{AP-res}	cm^{-3}	UHSAS	CVI	P6	80-1000 nm
Refractory black carbon particles, rBC						
rBC mass concentration	M_{rBC}	ng m^{-3}	SP2	Total	P6	73-575 nm
rBC number concentration	N_{rBC}	cm^{-3}	SP2	Total	P6	73-575 nm
rBC mass-equivalent diameter	D_{rBC}	nm	SP2	Total & CVI	P6	73-575 nm
rBC geometric mean diameter	$D_{rBC-Geo}$	nm	SP2	Total & CVI	P6	73-575 nm
rBC modal diameter	$D_{rBC-Mod}$	nm	SP2	Total & CVI	P6	73-575 nm
rBC residual mass concentration	M_{rBC}	ng m^{-3}	SP2	CVI	P6	73-575 nm
rBC residuals number concentration	$N_{rBC-res}$	cm^{-3}	SP2	CVI	P6	73-575 nm
Cloud particles						
Droplet number concentration	N_{Dro}	cm^{-3}	SID-3	-	P6	5-45 µm
Droplet number concentration, D > 10 µm	N_{Dro10}	cm^{-3}	SID-3	-	P6	10-45 µm
Liquid water content	LWC	g m^{-3}	SID-3	-	P6	5-45 µm
Ice water content	IWC	g m^{-3}	CIP	-	P6	75-1550 µm
Ice water fraction	IWF	-	CIP - SID-3	-	P6	5-1550 µm
Clout top height	-	m asl	AMALi	-	P5	-

810
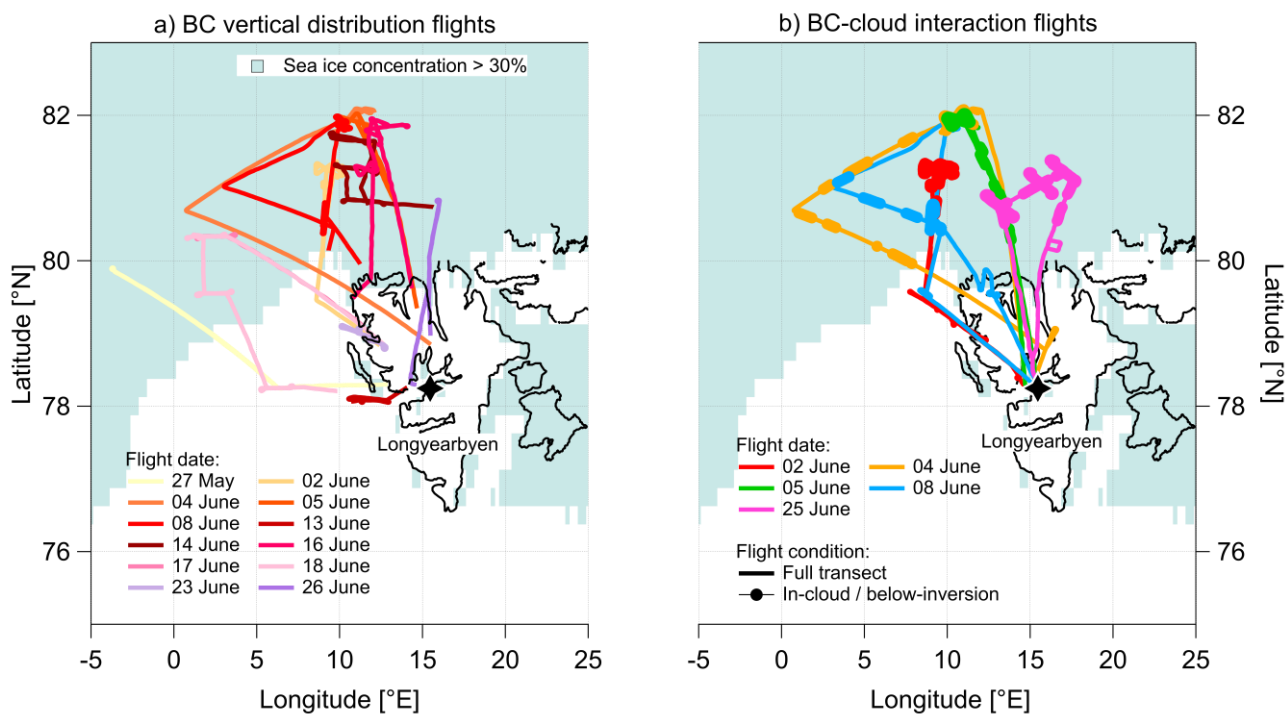
Figures

Figure 1 Map of Svalbard including flight patterns of the Polar 6 aircraft for the flights dedicated to investigating the vertical distribution (a) and cloud interaction (b) of BC particles. Sea ice concentration derived from the GHRSST Sea Surface Temperature Level 4, MUR25 sea surface temperature analysis product with 0.25° resolution (MUR-JPL-L4-GLOB-v4.1 doi:10.5067/GHGMR-4FJ04).

815
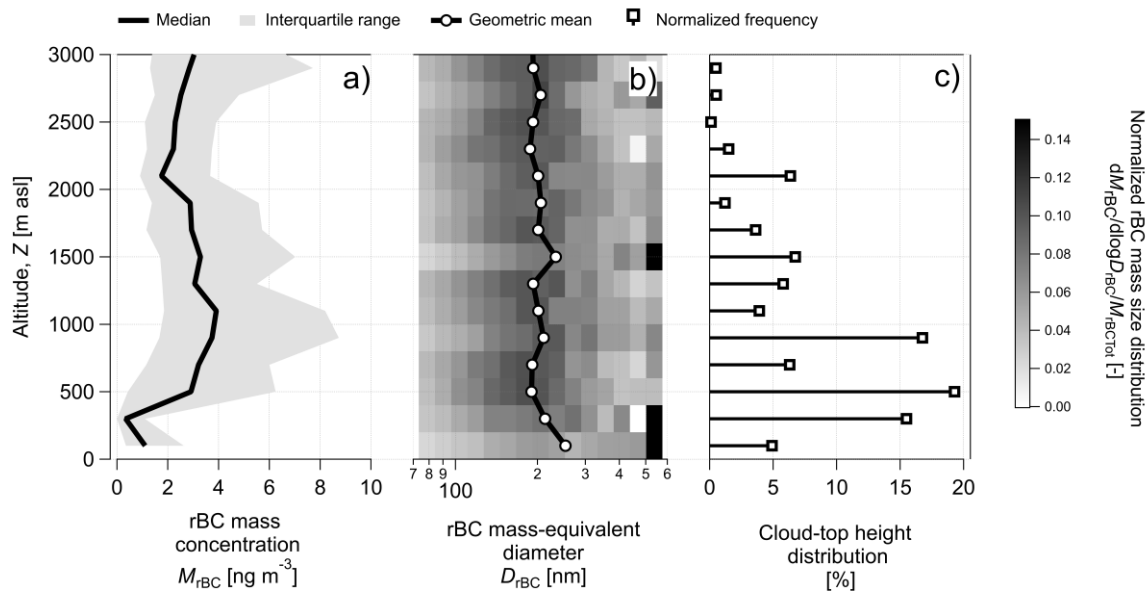
Figure 2 Vertical variability of: a) rBC mass concentration; b) rBC mass size distribution; c) cloud top height. rBC particles sampled behind the aerosol inlet and measured with the SP2 in the 75-575 nm diameter range. Cloud top derived from the AMALI instrument. Statistics calculated for equidistant altitude steps starting at the surface (0m asl) and 100m thick.
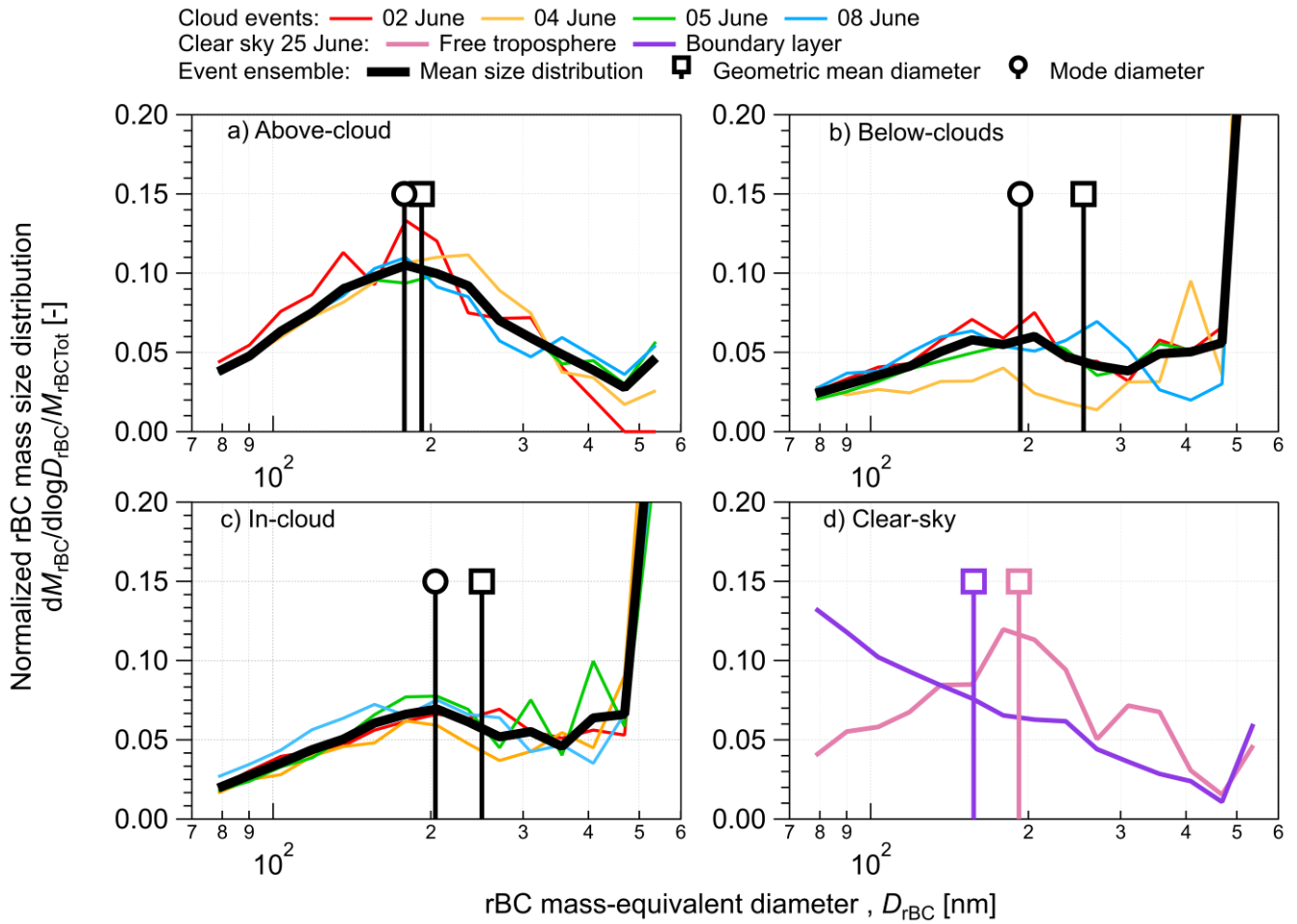
825

Figure 3 rBC normalized mass size distribution observed in: a) above cloud; b) below clouds; c) in cloud; d) clear sky. rBC particles measured in the 73-575 nm diameter range with the SP2. rBC in cloud sampled behind the CVI inlet, otherwise behind the total inlet.
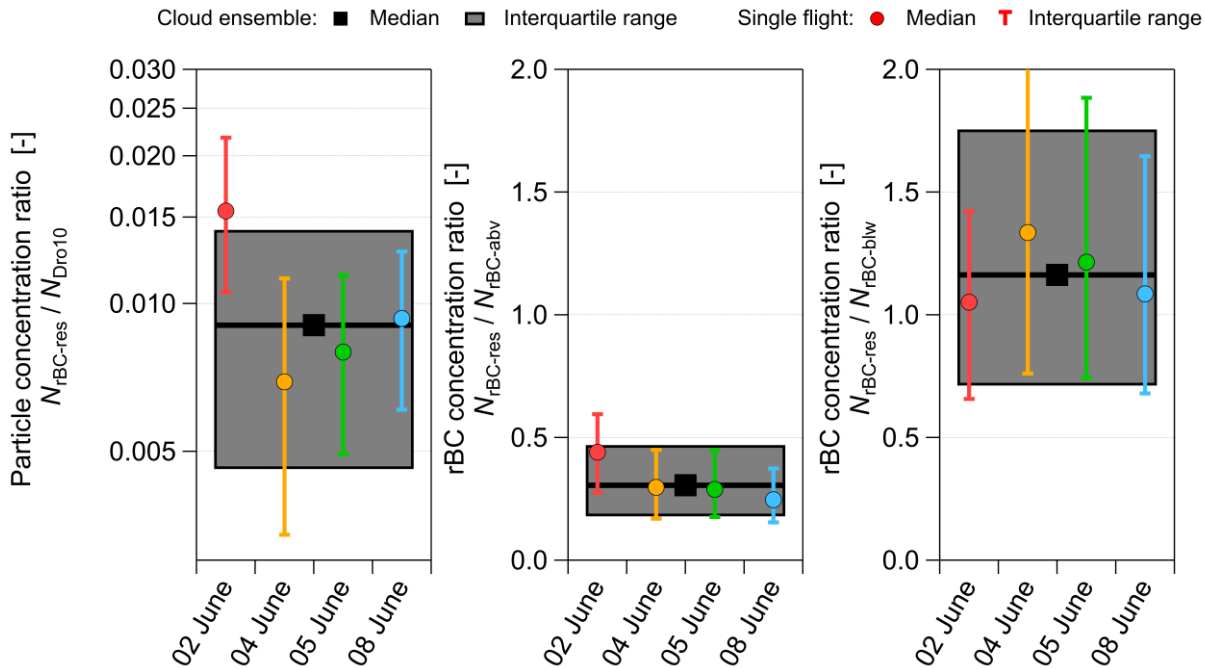
Figure 4 Box-plot of rBC concentration in cloud residuals. a) Ratio between the number concentration of cloud residuals ($N_{rBC\text{-}res}$) and the liquid droplet number concentration (N_{Dro10}). b) Ratio between the number concentration of cloud residuals ($N_{rBC\text{-}res}$) and the number concentration of rBC particles measured above cloud ($N_{rBC\text{-}Abv}$). c) Ratio between the number concentration of cloud residuals ($N_{rBC\text{-}res}$) and the number concentration of rBC particles measured below cloud ($N_{rBC\text{-}blw}$). Liquid droplets measured with the SID-3 probe in the 10-45 µm diameter range. rBC residuals sampled behind the CVI inlet or behind the total inlet and measured with the SP2 in the 73-575 nm diameter range.
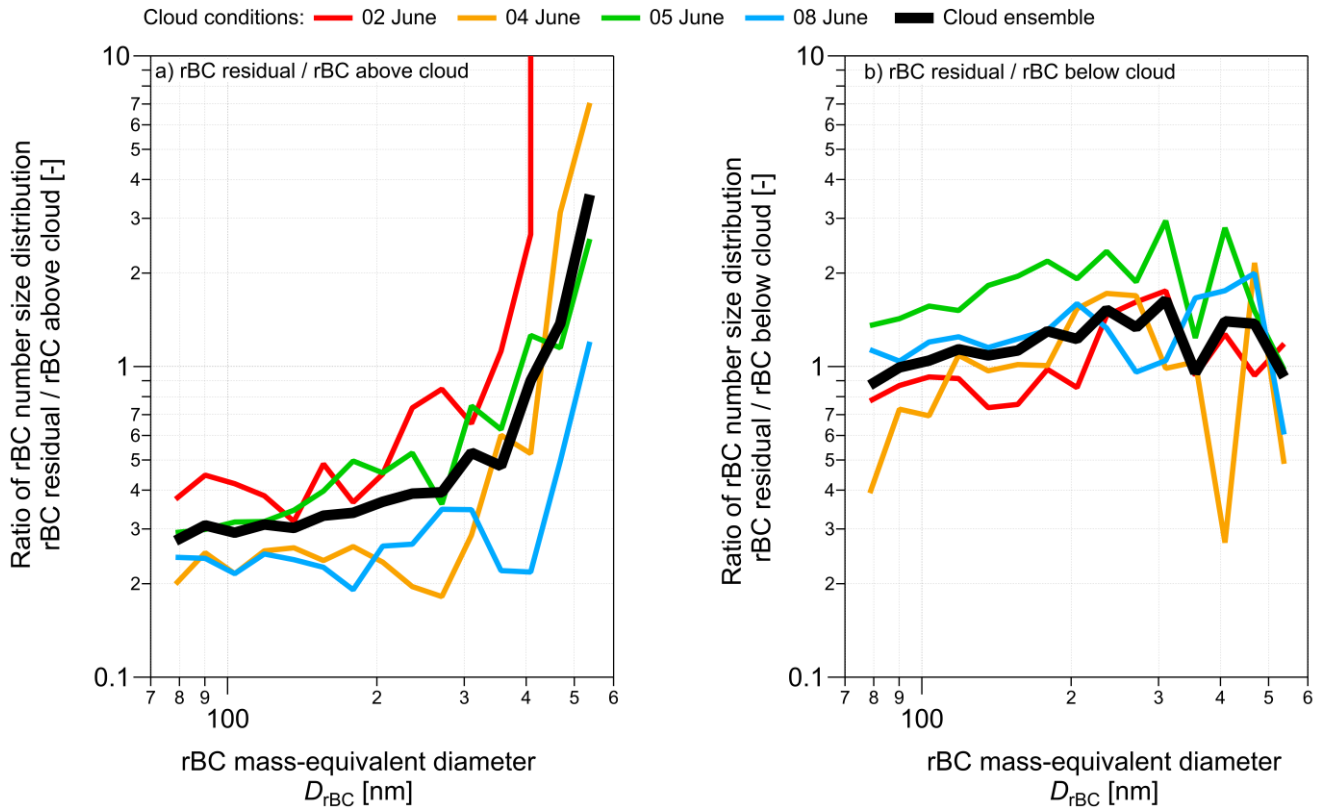
840

Figure 5 Ratio of number size distribution of rBC residuals over number size distribution of rBC particles sampled above cloud (a) and below cloud (b). rBC residuals sampled behind the CVI inlet, rBC particles sampled behind the total inlet. All rBC measured with the SP2 in the 73-575 nm diameter range.
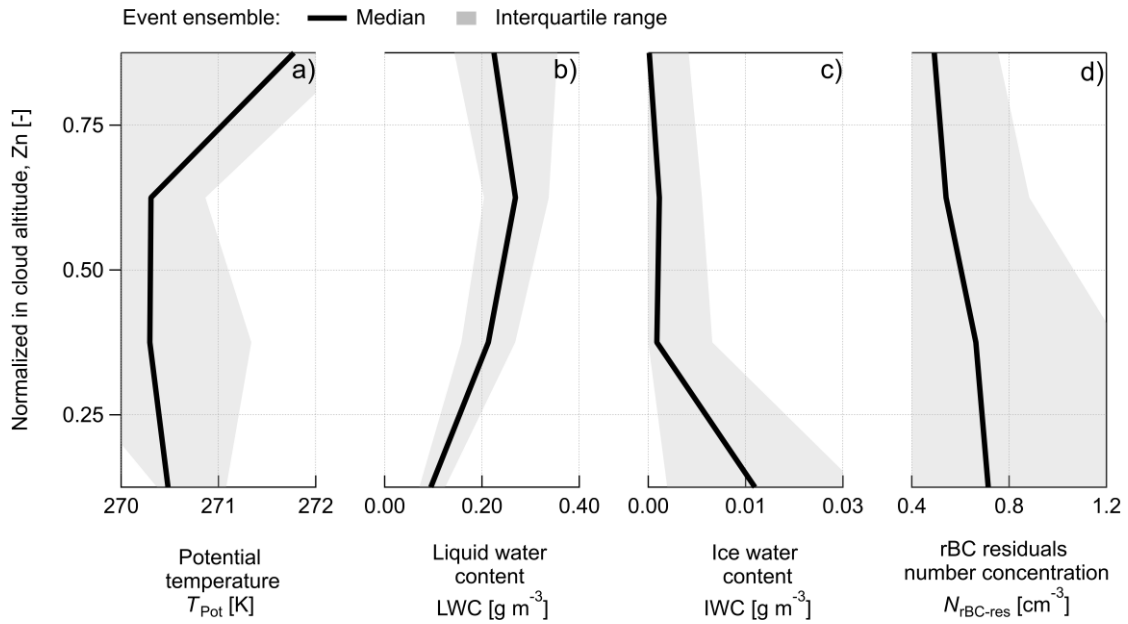
845

Figure 6 Vertical profiles of the cloud ensemble: a) Potential temperature, T_{Pot}; b) liquid water content, LWC; c) Ice water content, IWC; d) rBC-residual number concentration, $N_{rBC-res}$. Median and interquartile range calculated for in-cloud equidistant normalized altitude (Zn) steps of 0.25. Liquid droplets measured with the SID-3 probe in the 5-45 µm diameter range. Ice crystals measured with the CIP probe in the 75-1550 µm diameter range. rBC residuals sampled behind the CVI inlet and measured with

850 **the SP2 in the 73-575 nm diameter range.**
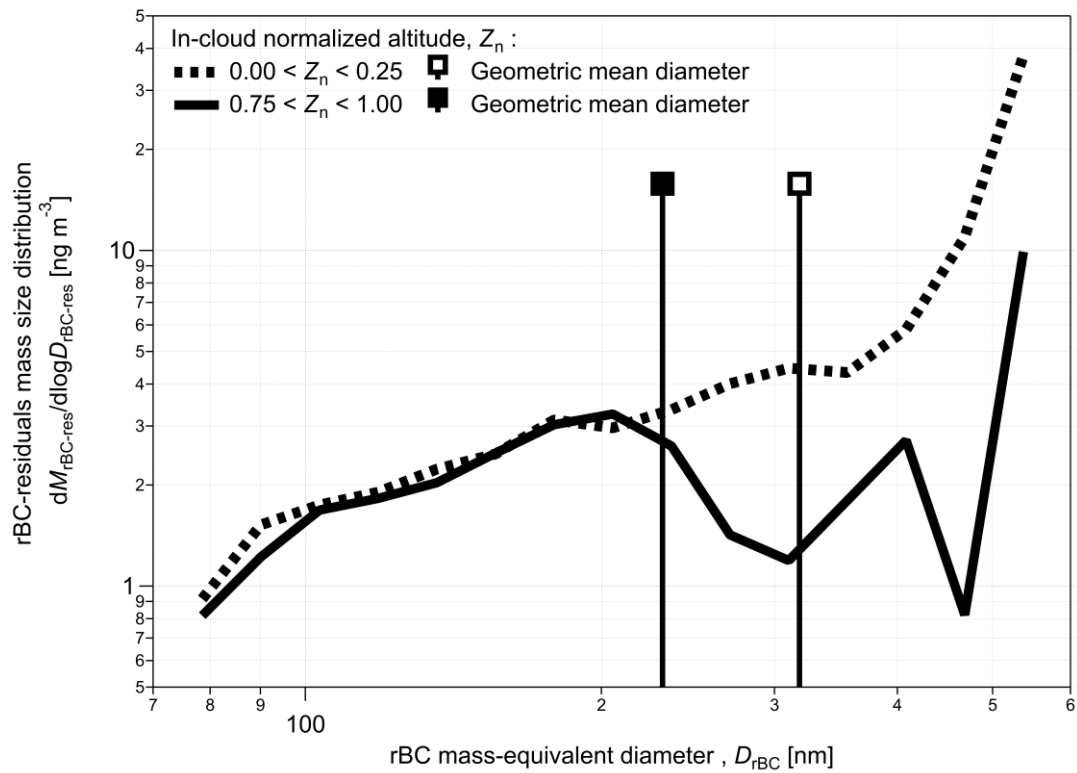
Figure 7 Mass size distribution of rBC residuals measured at cloud-top ($0.75 < Z_n < 1.00$) and cloud-bottom ($0.00 < Z_n < 0.25$). rBC
residuals sampled behind the CVI inlet and measured with the SP2 in the 73-575 nm diameter range.

855

Supplementary

CLOUD DESCRIPTION

860 The boundary layer was well defined by a marked inversion, similar to Brooks et al. (2017), located at 400 - 500 m asl, where potential temperature (T_P) increased by approximately 269-273 K to approximately 277-282 K (Figure S1a). The cumulative mean of T_P from the cloud base to the lowest sub-cloud measurement was compared with T_P calculated for each layer below-cloud. In general, the T_P difference never exceeded 0.5 K, suggesting the presence of surface-coupled clouds (Gierens et al., 2020) and the establishment of a well-mixed boundary layer (Shupe et al., 2013). A moist atmospheric layer (RH > 80%) was

865 confined by the inversion with values up to 98-100% between approximately 200 m asl and 500 m asl, while drier air (20% < RH < 50%) was observed above 500 m asl (Figure S1b). Within this moist boundary layer, liquid droplets were observed from a maximum altitude of 500 m asl to a minimum altitude of 50-60 m asl (Figure S1c). Following the work of Sedlar et al. (2011), these cloud cases can be classified as cloud inside inversion, since the cloud top height extended above inversion-base height but below inversion-top height. Ice crystals with diameter larger than 75 μm measured with the CIP probe were observed

870 across the cloud layer to the lowermost altitude below cloud base, indicating the presence of mixed phase clouds and, ice precipitation below cloud base during all selected flights (Figure S1d). Overall, the vertical atmospheric structure remained quite similar from 02 to 08 June, confirming the establishment of stable atmospheric conditions maintaining mixed-phase clouds in the boundary layer, as expected in Arctic summer conditions (Morrison et al., 2012). Valid measurements of cloud residuals ranged from a maximum altitude of 544 m asl on 05 June to a minimum altitude of 60 m asl on 04 June. Overall, the

875 vertical thickness of residual measurements varied from 310 m to 435 m, accounting for a total of 197 minutes. Above-cloud observations of aerosol particles were performed above the cloud-top and inversion layer in the 400-750 m altitude range. The vertical range covering the below-cloud bottom was very thin (100 - 150 m) and is considered to be representative of Arctic boundary layer impacted by mixed-phase clouds.
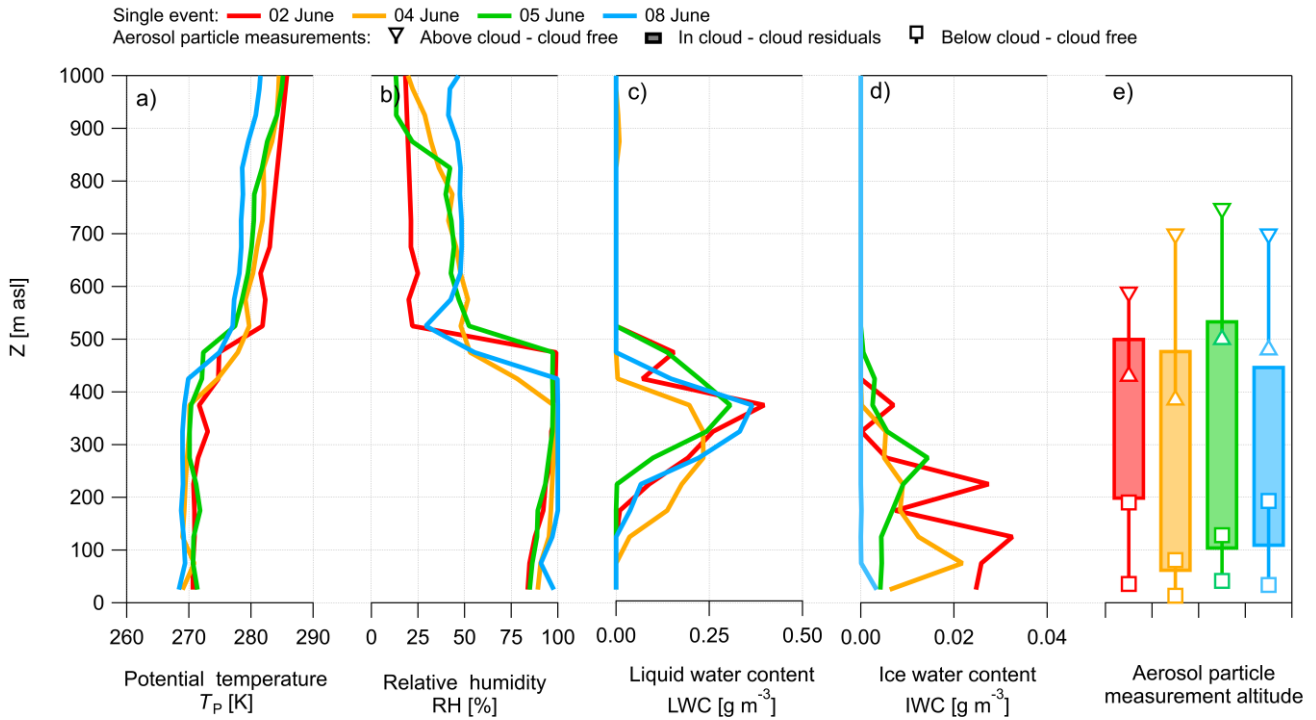
880 **Figure S1 Atmospheric and cloud characterisation of four flights occurred on 2, 4, 5 and 8 June 2017 (warm-period) north-west of Svalbard. Median vertical profile of: a) potential temperature, TP; b) relative humidity, RH; c) number concentration of droplets, N_{Dro}; d) number concentration of ice crystals, N_{Ice}; e) altitude range of aerosol particle measurement in different conditions. Liquid droplets measured with the SID-3 probe in the 5-45 µm diameter range. Ice crystals measured with the CIP probe in the 75-1550 µm diameter range. Statistics calculated for equidistant altitude steps starting at the surface (0m asl) and 50 m thick.**

885

COATING THICKNES DISTRIBTUION
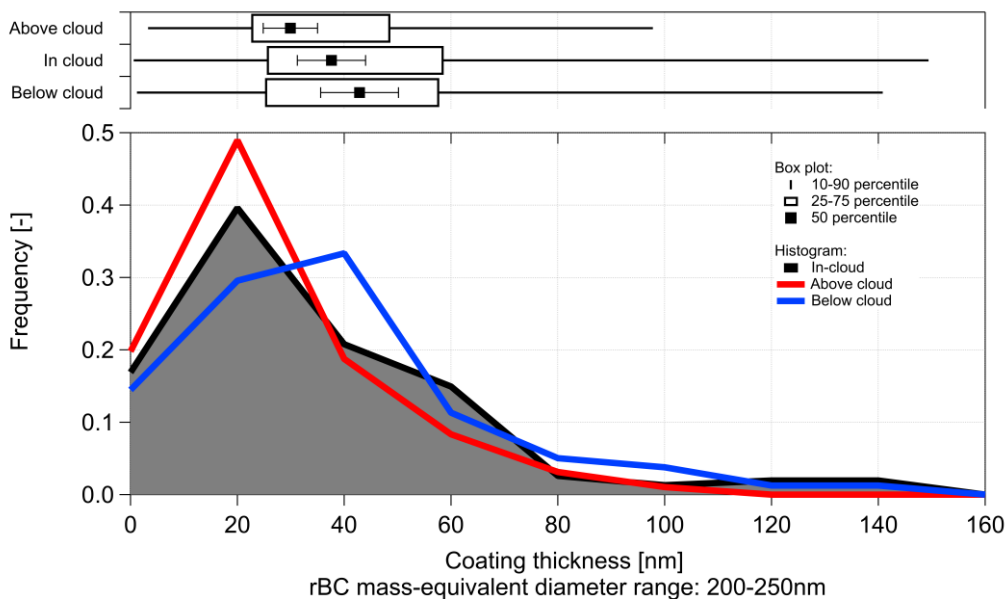
Figure S2 Coating thickness distribution calculated for rBC particles with a mass equivalent diameter in the 200-250 nm range. Coating thickness data available only for the flight occurred on 02 June 2017.

890

VERTICAL VARIABILITY OF CLOUD PARTICLES
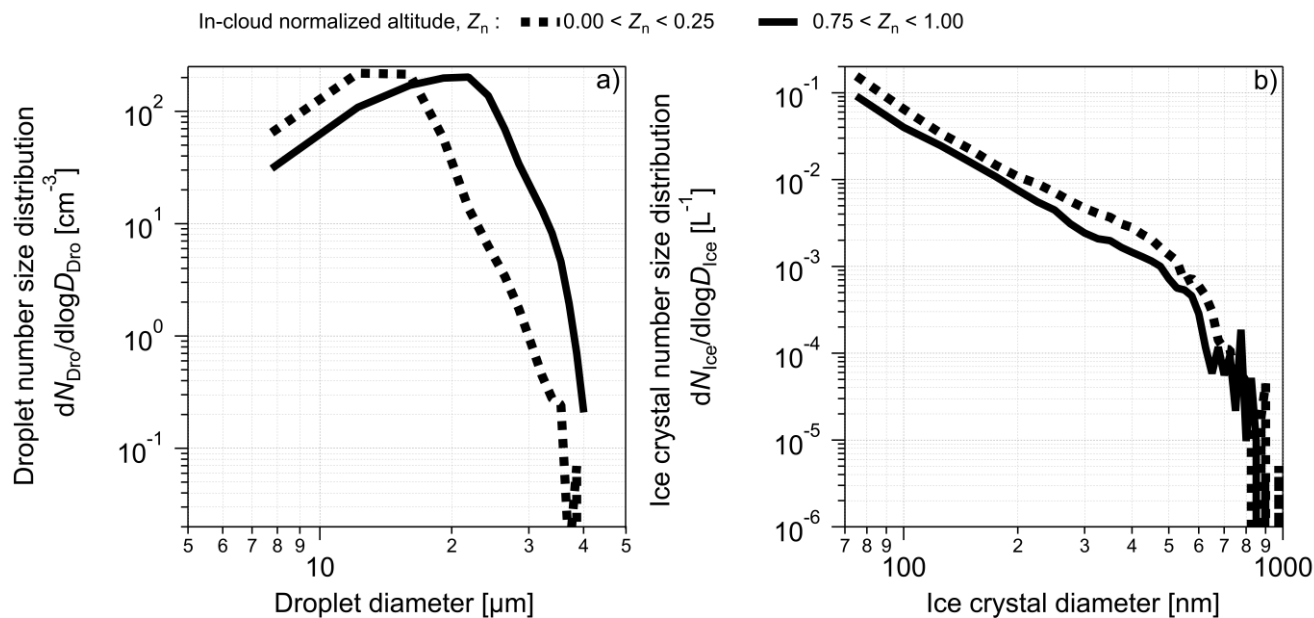
Figure S3 Size distribution of: a) liquid droplets measured with the SID-3 in the 10-45 μm diameter range; b) ice crystals measured with the CIP in the 75-1550 μm diameter range